DEPARTAMENT OF MATERIALS SCIENCE

FRANCISCA FRAÚSTO FREIRE DA CRUZ

BSc in Materials Science and Engineering

MULTIFUNCTIONAL SUPERPARAMAGNETIC MESOPOROUS BIOACTIVE GLASS-BASED INJECTABLE BONE CEMENTS FOR CANCER THERANOSTICS AND BONE REGENERATION

INTEGRATED MASTER IN MATERIALS ENGINEERING

NOVA University Lisbon

September, 2024

DEPARTAMENT OF MATERIALS SCIENCE

MULTIFUNCTIONAL SUPERPARAMAGNETIC MESOPOROUS BIOACTIVE GLASS-BASED INJECTABLE BONE CEMENTS FOR CANCER THERANOSTICS AND BONE REGENERATION

FRANCISCA FRAÚSTO FREIRE DA CRUZ

BSc in Materials Science and Engineering

Adviser: Professor Doutor João Paulo Borges
Full Professor, NOVA School of Science and Technology, Lisbon

Co-adviser: Doutora Paula Soares
Principal Researcher, NOVA School of Sciences & Technology, Lisbon

Examination Committee:

Chair: Professor Doctor Maria Margarida Rolim Augusto,
Assistant Professor in the Department of Materials Science at NOVA School of Science and Technology | NOVA FCT

Rapporteurs: Professor Doctor Jorge Alexandre Monteiro de Carvalho e Silva,
Associate Professor of the Department of Physics at NOVA School of Science and Technology | NOVA FCT

Adviser: Professor Doctor João Paulo Borges,
Full Professor of the Department of Materials Science at NOVA School of Science and Technology | NOVA FCT

INTEGRATED MASTER IN MATERIALS ENGINEERING

NOVA University Lisbon
September, 2024

Multifunctional superparamagnetic mesoporous bioactive glass-based injectable bone cements for cancer theranostics and bone regeneration

À minha tia Ana.

ACKNOWLEDGEMENTS

Agradeço profundamente aos meus orientadores, Professor João Paulo Borges e Doutora Paula Soares, pelo incentivo constante desde o início deste projeto, por todas as vezes em que lhes bati à porta com dúvidas ou problemas e estiveram sempre prontos a ajudar, e por toda a sabedoria que me transmitiram.

Um obrigada á Professora Catarina Leal do ISEL por todo o tempo despendido no reómetro e por toda a aprendizagem sobre reologia.

Gostaria de agradecer também às colegas de doutoramento Sofia e Adriana, Sofia por todo e longo trabalho de bioatividade e citotoxicidade com os MBG e cimentos, e Adriana pelo SEM e por todas as dicas de laboratório ao longo do semestre.

Ao meu Padrinho Hélder pelos conselhos e aos meus colegas de laboratório: Alexandra, que me acompanhou quase lado a lado no processo de produção. Não foi fácil, mas sem ela tinha sido ainda mais difícil e a verdade é que conseguimos. Obrigada. E Miguel por todo o apoio e noitadas a trabalhar.

Aos meus pais, os que mais acreditam em mim e me apoiam incondicionalmente. Um obrigada também á minha família, Avó, Tia Graça, Paula, Tio Paulo, Manos e Sobrinhas.

Á minha base, os meus amigos Ana, Érica, Sara e Guilherme, obrigada por estarem sempre lá para mim.

Por fim, mas não menos importante ao meu namorado Manuel, que teve muito de aturar com esta tese, mas que nunca me que fez perder a motivação, pelo contrário. Muito obrigada.

“There are things known and there are things unknown, and in between are the doors of perception.” (Aldous Huxley).

ABSTRACT

Bone cancer treatment often involves invasive surgeries and non-specific therapies like chemotherapy and radiotherapy, which can lead to severe side effects and incomplete tumour removal. This thesis explores the development of multifunctional injectable bone cement based on superparamagnetic mesoporous bioactive glass (MBG) for cancer theranostics and bone regeneration. The cements incorporate superparamagnetic iron oxide nanoparticles (SPIONs) to enable localized hyperthermia, and therapeutic ions such as copper (Cu^{2+}) to provide antibacterial, osteogenic, and angiogenic properties. The research focuses on optimizing the synthesis of MBGs with varying Cu^{2+} contents (0%, 2%, and 5%) and their subsequent functionalization with SPIONs (SPIONs@MBG). Extensive characterization revealed that the inclusion of Cu^{2+} influences the structural and biological properties of the MBGs, enhancing their bioactivity and antibacterial efficacy, particularly against Gram-positive bacteria. The rheological properties and setting times of the injectable cements were tailored by adjusting the liquid-to-solid (L/S) ratio, ensuring optimal injectability and mechanical stability for clinical applications. Cytotoxicity tests using human osteosarcoma cells (Saos-2) indicated that the MBG exhibit good biocompatibility, with cell viability above 70% for most compositions. Magnetic hyperthermia tests demonstrated that SPIONs@MBGs could achieve localized heating, though further optimization is required to reach therapeutic temperature ranges. These findings suggest that SPIONs@MBG-based cements hold significant potential as multifunctional materials for bone cancer treatment, offering a synergistic approach that combines targeted hyperthermia and regenerative capabilities. Future work will focus on in vivo studies to assess the clinical efficacy of these injectable cements for bone regeneration and localized cancer therapy.

Keywords: Bone Cement, Bone Regeneration, Cancer Theranostics, Mesoporous Bioactive Glass, Superparamagnetic Nanoparticles.

RESUMO

O tratamento do cancro ósseo envolve frequentemente cirurgias invasivas e terapias inespecíficas, como quimioterapia e radioterapia, que podem causar efeitos secundários graves e resultar numa remoção incompleta do tumor. Esta tese explora o desenvolvimento de cimentos ósseos injetáveis multifuncionais baseados em vidro bioativo mesoporoso superparamagnético (MBG) para teranóstico do cancro e regeneração óssea. Estes cimentos incorporam nanopartículas superparamagnéticas de óxido de ferro (SPIONs) para permitir hipertermia localizada, juntamente com iões terapêuticos como o cobre (Cu^{2+}), que conferem propriedades antibacterianas, osteogénicas e angiogénicas. A investigação centra-se na síntese de MBGs com diferentes teores de Cu^{2+} (0%, 2% e 5%) e na sua funcionalização com SPIONs (SPIONs@MBG). A inclusão de Cu^{2+} melhora as propriedades bioativas e antibacterianas dos MBGs, especialmente contra bactérias Gram-positivas. As propriedades reológicas e os tempos de presa dos cimentos foram ajustados através da razão líquido-sólido (L/S), assegurando injetabilidade e estabilidade mecânica adequadas para aplicações clínicas. Testes de citotoxicidade em células humanas de osteossarcoma (Saos-2) indicaram boa biocompatibilidade, com viabilidade celular superior a 70% na maioria das composições. Os testes de hipertermia magnética mostraram que os SPIONs@MBGs podem alcançar aquecimento localizado, embora seja necessária uma otimização adicional para atingir temperaturas terapêuticas. Estes resultados sugerem que os cimentos baseados em SPIONs@MBG têm potencial como materiais multifuncionais para o tratamento do cancro ósseo, combinando hipertermia direcionada e regeneração óssea. Estudos futuros avaliarão a eficácia clínica destes cimentos na regeneração óssea e na terapia localizada do cancro.

Palavas chave: Cimento Ósseo, Nanopartículas Superparamagnéticas, Regeneração Óssea, Teranóstica do Cancro, Vidro Bioativo Mesoporoso.

CONTENTS

LIST OF FIGURES

LIST OF TABLES

ABBREVIATIONS

AMF	Alternating Magnetic Field
BJH	Barrett-Joyner-Halenda
BG	Bioactive Glass
EISA	Evaporation-induced Self-assembly
FTIR	Fourier-transform Infrared Spectroscopy
MBG	Mesoporous Bioactive Glass
MIC	Minimum Inhibitory Concentration
HA	Hydroxyapatite
HCA	Hydroxycarbonate Apatite
ICP	Inductively Coupled Plasma
ROS	Reactive Oxygen Species
SAED	Selected Area Electron Diffraction
SBF	Simulated Body Fluid
SDBG	SPION-deposited Bioactive Glass
SEBG	SPION-embedded Bioactive Glass
SEM	Scanning Electron Microscopy
SPION	Superparamagnetic Iron Oxide Nanoparticle
SPIONs@MBG	SPIONs deposited on Mesoporous Bioactive Glass
STEM	Scanning Transmission Electron Microscopy
XRD	X-ray diffraction

1

MOTIVATION

Bone tumors usually occur in the bone or its associated tissues and are often characterized by pain and bone destruction. Researchers are actively exploring new approaches to identify the most effective treatments, and today, the most common are based on surgery, chemotherapy, and radiotherapy. However, in certain cases, surgery may not be able to completely remove the tumor cells. Although radiotherapy and chemotherapy are the most commonly used methods to destroy and remove cancer cells, they are not always the most effective or appropriate, as they inevitably damage healthy cells as well [1]. As a result, oncologists are increasingly turning to more sophisticated and innovative therapies, moving away from conventional chemotherapy and radiotherapy in favor of targeted therapy. However, this shift does not mean that chemotherapy and radiotherapy should be completely abandoned; instead, these treatments could be complemented by other strategies and used in a complementary manner.

One potential complementary strategy is the use of hyperthermia, i.e., raising the temperature at the affected site above 40 ºC to eliminate cancer cells [2], which offers advantages including the absence of harmful radiation. Another alternative to these approaches is the local injection of cements based on superparamagnetic multifunctional Mesoporous Bioactive Glasses (MBG). These cements fill the defects, self-set *in situ,* and, when combined with a treatment approach, can stop the uncontrolled growth of abnormal cells by eliminating the cancer cells.

The incorporation of therapeutic ions such as Cu^{2+}, Zn^{2+}, and Mg^{2+} into the Bioactive Glass (BG) imparts multifunctionality, providing antibacterial, osteogenic (ability to stimulate the formation of new bone tissue), and angiogenic (formation of new blood vessels) activities. Mesoporosity (nanometer-sized pores) enhances biological activity by increasing the surface area, which is critical for BG [3]. In addition, the superparamagnetic properties in MBG can be used to treat cancer through magnetic hyperthermia [2].

Despite all the obstacles and limitations to be overcome, this project aims to develop an injectable bone cement based on superparamagnetic mesoporous bioactive glasses. Cu^{2+} is known to simultaneously impart antibacterial, osteogenic, and angiogenic activity to BG, and therefore, its use as a therapeutic ion will be investigated. Few studies have been carried out on superparamagnetic iron oxide nanoparticles (SPIONs) incorporated into MGBs, so we will investigate the effect of SPION-deposited bioactive glasses (SDBGs), as they seem to have better magnetic properties. This document is divided into four sections. Section 2 introduces the topic, covering the concepts of BG, MBG, their applications in magnetic hyperthermia and bone regeneration, as well as the effects of copper doping and its therapeutic and biological properties. Section 3 provides a detailed overview of the materials and methods used in this project. Section 4 presents the results obtained, including their discussion and comparison with existing literature. Section 5 presents conclusions and future perspectives, and the appendix contains supplementary information to all sections.

2

INTRODUCTION

2.1 Bioactive Glasses

The first BG ever produced, called 45S5 Bioglass®, was discovered in 1969 by Prof. Larry Hench at the University of Florida with a chemical composition of $45SiO_2$–24.5CaO–24.5NaO–$6P_2O_5$ (wt%). Since then, BGs have been extensively studied due to their unique ability to chemically bond with living bone tissue, making them very valuable in medical applications. This property has led to their use in clinical bone repair implants, tissue engineering coatings, drug delivery devices, and tumor treatment [4]. The prerequisite for these materials to bond with living bone is the formation of a biologically active hydroxycarbonate apatite (HCA) layer on their surface when exposed to physiological fluids. This HCA surface layer allows BGs to interact with cells and adjacent tissues, promoting various cellular functions [5]. *In vivo* implantation experiments show that BGs with specific compositions do not exhibit local or systemic toxicity, inflammation, or foreign body reaction. They effectively bind to both soft and hard tissues without forming an intervening fibrous layer [6].

2.2 Mesoporous Bioactive glasses

In 2004, highly ordered MBGs (SiO_2-CaO-P_2O_5) [7] were synthesized for the first time by using non-ionic block copolymers as structure-directing agents through an evaporation-induced self-assembly (EISA) process [8]. One way to accelerate the kinetic deposition process of HCA is to increase the specific surface area and pore volume of BGs. Studies show that mesopore sizes larger than 2 nm promote faster crystallization of HCA [6].

In order to produce well-ordered MBGs, it is now essential to incorporate surface-active agents such as Pluronic P123 and F127. These surfactants play a key role in organizing themselves into micelles under specific synthesis conditions. Micelles are aggregates of surfactant molecules with a hydrophobic core and a hydrophilic shell. The micelles then act as a binding framework for the hydrolyzed silica precursors through their hydrophilic components, leading to the self-assembly of a structured mesophase. The mesophase, which is a liquid or gel-like intermediate structure with ordered arrangements of micelles and silica components, is then subjected to an EISA process. During this process, the solvent (typically ethanol or another volatile solvent) in the mixture is gradually evaporated, and the structured mesophase undergoes further self-assembly. When the mixture is dried and the surfactant removed, the result is a well-ordered mesoporous structure characterized by high surface area and high porosity [3] [8]. The synthesis method for MBGs produces materials with consistent and controllable pore sizes, substantial pore volumes, and high *in vitro* bioactivity. The calcination temperature plays a crucial role in determining the *in vitro* bioactivity of MBGs. Studies indicate that calcining MBGs at 700°C may result in optimal *in vitro* bioactivity [6].

Scanning electron microscopy (SEM) results from an experimental study comparing mesoporous bioactive glasses (MBGs) with varying compositions showed that in vitro bioactivity followed this sequence: 80S15C > 70S25C > 60S35C > 95S5C > 100S. Here, S represents the percentage of silica content, and C represents the percentage of calcium oxide, with the 80S15C composition demonstrating the highest bioactivity [9]. The typical oxides incorporated in the silicate BGs impart specific properties to the material: for example, Na_2O and CaO are useful to adjust the surface reactivity in the biological environment, and B_2O_3 is known for its high reactivity, which accelerates the bioactive response kinetics [10]. A current method of improving the properties of MBGs is the incorporation of therapeutic ions. The substitution of small amounts of oxides serves to enhance osteogenesis, antibacterial efficacy, angiogenesis, and the overall effects of MBGs [10].

2.3 Magnetic Bioglasses in Magnetic Hyperthermia and Regeneration

As mentioned earlier, hyperthermia, a promising technique, uses elevated temperatures (typically 40-43°C) to selectively eliminate malignant cells while sparing normal tissue. In magnetically induced hyperthermia, superparamagnetic materials (called thermoseeds) are injected into tumor cells, and the system is exposed to externally applied alternating magnetic fields (AMF), resulting in the destruction of the respective cancer cells [11].

The use of superparamagnetic iron oxide nanoparticles (SPIONs), such as magnetite [Fe_3O_4] or maghemite [γ-Fe_2O_3], has been proposed because they generate heat when exposed to an AMF, leading to local hyperthermia [12]. They must be 20 nm or less to become superparamagnetic. They exhibit zero coercivity and zero remanence, meaning they do not retain any magnetization once the external magnetic field is removed. This property allows precise control of their magnetic behavior, making them suitable for targeted medical applications. However, several challenges limit the effectiveness of SPIONs as thermoseeds in anti-cancer therapies. A major concern is the dissolution of SPIONs, which can release iron particles in the body and potentially promote tumor growth. Additionally, SPIONs are prone to agglomeration when subjected to AMF. This agglomeration is driven by their high surface energy, which is a consequence of their high surface area-to-volume ratio. Furthermore, attractive magnetic and van der Waals forces cause individual particles to cluster together [13].

These problems can be overcome by coating or functionalizing the surface of the SPIONs. An innovative solution is to combine BG nanoparticles with SPIONs, providing a synergistic approach that allows the superparamagnetic properties of SPIONs to be exploited together with the exceptional features of BGs. This combination not only enhances the therapeutic potential of BGs, promoting bone tissue regeneration but also serves to protect SPIONs from undesirable side effects. Looking for a way to integrate sol-gel synthesized BGs and SPIONs, two different methods were investigated to create the desired composite nanoparticles. In the first method, SPIONs were incorporated inside the BG nanoparticles, resulting in so-called SPION-embedded bioactive glass (SEBG) nanoparticles. Alternatively, in the second method, SPIONs were deposited onto the bioactive glass nanoparticles, like a thin shell, resulting in SPION-deposited bioactive glass (SDBG) nanoparticles [12]. At the laboratory level, measurements were carried out to characterize and compare the magnetic properties of SPIONs, SEBGs, and SDBGs. Although the saturation magnetization (M_s) values for these composite nanoparticles were lower than those of SPIONs, they still exhibited superparamagnetic behaviour suitable for biomedical applications, with properties of zero coercivity and remanence at room temperature. The magnetization value for SDBG nanoparticles was more than twice that of SEBG nanoparticles due to the thicker bioactive glass layer surrounding the embedded SPIONs and a reduced number of SPIONs inside SEBG [12].

2.4 Copper-doped BGs/MBGs

Copper, an element naturally present in the human body, has attracted much attention due to its vital role in various metabolic processes. At appropriate levels, it is not harmful to human tissues, but it has potent effects on microorganisms. Numerous studies have demonstrated the antibacterial, osteogenic, and angiogenic efficacy of MBGs doped with copper oxide (CuO). The sustained release of Cu^{2+} ions from sol-gel-derived MBGs ensures long-term therapeutic effects. The versatility of copper-doped MBGs allows their properties to be tailored for specific applications. Their broad-spectrum antibacterial activity extends to different bacterial strains, making copper a promising therapeutic ion for biomedical applications [10].

Recent research by Gupta and colleagues explored the impact of Cu^{2+}, Ag^{+}, and Fe^{3+} ions as dopants on the structural, mechanical, and antibacterial properties of BGs for potential use in bone tissue engineering. Copper-substituted MBGs exhibited higher antibacterial efficacy compared to other substituted ions. In another study, Koohkan and team prepared two Cu-containing MBGs with and without surfactant (P123), named Cu-PBG and Cu-BG, respectively, using the sol-gel method. Cu-PBG exhibited enhanced bactericidal efficacy against Gram-negative E. coli, which was attributed to its higher initial release of Cu and Ca ions compared to Cu-BG within the first 24 hours. This phenomenon is a result of the increased specific surface area of the surfactant-templated mesoporous material compared to the conventional sol-gel BG, which facilitates accelerated ion exchange in the test medium. In further research, Bari and colleagues conducted a study on copper-containing MBG nanoparticles designed as a multifunctional agent for bone regeneration. They formulated MBGs with a Si/Ca ratio of 85/15 (mol%) and modified them by substituting copper ions for calcium. The MBGs with 2 mol% Cu demonstrated a higher exposed surface area of 550 $m^2\ g^{-1}$ and a pore volume of 0.26 $cm^3\ g^{-1}$, compared to those with 5 mol% Cu, which exhibited a surface area of 224 $m^2\ g^{-1}$ and a pore volume of 0.11 $cm^3\ g^{-1}$. This indicates the significant role of copper in influencing the textural properties of the material. The increased surface area and the presence of mesopores, enhanced the *in vitro* bioactive response and enabled a sustained release of Cu^{2+} ions. This, in turn, resulted in a greater antibacterial effect against various bacterial species, including E. coli, S. aureus, and S. epidermidis. Thus, the incorporation of 2 mol% Cu into MBGs improved their structural characteristics and amplified their biological activity, making them a promising agent for bone regeneration applications [14]. In a different investigation, copper oxide was introduced into iron-containing BGs to examine its influence on the magnetic characteristics of the glasses. The incorporation of copper into the iron-doped glasses not only increased the superparamagnetic properties of the samples from 0.236 emu/g to 1.043 emu/g but also contributed to the enhancement of these properties. This enhancement is attributed to the role of copper in facilitating the integration of iron oxide into the glass network, thereby promoting the improved formation of the crystalline phase of magnetite. Furthermore, the introduction of copper into the iron-doped BGs increased their bioactivity, cytocompatibility, and antibacterial efficacy which are crucial parameters in tissue engineering applications [15].

2.5 Magnetic Bioactive glasses

Mesoporous Magnetic Bioactive Glasses (MMBGs) hold significant promise for bone cancer treatment, as they integrate the biocompatibility and multifunctionality of MBGs with the superparamagnetic properties of SPIONs. However, there are few reports on their biological properties [16].

In one investigation, the effects of mesopores and Fe_3O_4 nanoparticles on the properties of drug loading, release, bactericidal activity, and biocompatibility were investigated. MBG, MMBG, and non-mesoporous bioactive glass (NBG) were used as control samples for comparison. Gentamicin was incorporated into the glasses to evaluate both drug loading and release. MMBG, fabricated using a non-ionic surfactant as a soft template, demonstrated superior drug delivery capabilities, bactericidal activity, and cytocompatibility compared to NBG. The ordered mesoporous structure of MMBG contributed to its high drug loading efficiency (65.6-68.6%), which outperformed NBG (14.3-19.6%). The mesoporous channels facilitated the entry of gentamicin molecules, and the high specific surface area provided ample binding sites for drug attachment. In addition, the large pore volume of MMBG accommodated a significant amount of gentamicin. *In vitro* drug release studies showed that both Gent-MMBG and Gent MBG exhibited slow and sustained release of gentamicin, maintaining concentrations above effective antibacterial levels for up to 6 days. The antibacterial properties of Gent-MMBG and Gent-MBG were particularly effective against Staphylococcus epidermidis and Staphylococcus aureus, common causes of implant-associated infections. The magnetic Fe_3O_4 nanoparticles in Gent-MMBG played a significant role in preventing biofilm formation, thereby enhancing the antibiotic properties. Despite the lower drug release of Gent-MMBG compared to Gent-MBG, gentamicin concentrations remained above the minimum inhibitory concentrations, demonstrating its sustained efficacy. Cytocompatibility assessments using human bone marrow-derived mesenchymal stem cells (hBMSCs) indicated that MMBG supported crucial cell functions, such as adhesion and proliferation [16]. Another study created mesoporous magnetic glass scaffolds in the Fe_3O_4–CaO–SiO_2–P_2O_5 system and demonstrated a reduced dissolution rate in physiological environments and improved osteoblast cell proliferation and differentiation when CaO was replaced by Fe_2O_3 [17].

2.6 Mesoporous Bioactive Glass Cement

A highly desirable feature of BG cement is its ability to initially form a plastic paste, allowing it to be easily injected and molded into irregularly shaped defects in bone and teeth. The ideal cement, exemplified by a mesoporous bioactive glass cement (MBGC), not only exhibits the desired plasticity but also has a rapid setting capability, allowing for efficient application and rapid setting over time [18].

In an experiment, an MBGC with the characteristics described above was successfully created. This innovative material consisted of highly ordered MBG powders as the solid component and an ammonium phosphate buffer solution as the liquid component. It was found that the rapid setting of MBGC is facilitated by the rapid formation of plate-like, calcium-deficient hydroxyapatite (HA) nanocrystals when the solid and liquid components are mixed. These HA nanocrystals act as linkers between the glass particles, enhancing the mechanical robustness of the MBGC. Upon immersion in simulated body fluid (SBF), the HA nanocrystals further stimulate the rapid precipitation and growth of crystalline HA layers [18].

MMBG has demonstrated multifunctionality with excellent drug delivery, antibacterial efficacy, and cytocompatibility. It appears to be a promising solution for the treatment of bone infections. However, further studies are recommended to evaluate its effect on different cell populations and to confirm its suitability for various biomedical applications [11]. MBGC, also at an early stage of research, can combine plasticity, rapid setting behavior, and superior *in vitro* bioactivity, making it a promising material for applications in clinical orthopedics, controlled drug delivery, and tissue engineering [18]

3

MATERIALS AND METHODS

Further information on the materials and characterization techniques employed in this work is provided in Sections A.1 (Materials) and A.2 (Characterization) of the Appendix.

3.1 Mesoporous Bioglasses (MBG) synthesis

Highly ordered mesoporous SiO_2-CaO-P_2O_5 sol-gel glasses were synthesized by a previously described EISA process [6]. In this procedure, a nonionic surfactant, Pluronic P123 was used as structure directing agent, and TEOS, calcium nitrate, and TEP were used as SiO_2, CaO, and P_2O_5 sources, respectively. Three different Cu contents (0, 2 and 5 mol%) were prepared by substituting portions of calcium in MBG. Briefly, to prepare MBG with 5% Cu, 8 g of P123, 21.44 mL of TEOS, 2.83 g of calcium nitrate ($Ca(NO_3)_2$), 1.02 g of copper(II) chloride ($CuCl_2$), 2.04 mL of TEP, and 1.68g of 0.5 M HCl were dissolved in 120 g of ethanol and stirred at 250 rpm for 72 hours at room temperature (Figure 1(a)). The gel was then dried at 80 °C for 72 hours and finally treated at 700 °C for 5 hours to obtain the final calcined glass powder (Figure 1(b)). MBG without Cu and with 2% Cu were prepared using the same method. The molar ratios and amounts of reactants used in this synthesis are documented in Table 1. To homogenize and reduce the particle size of the obtained BG powder, the powder was ground in a Planetary Mono Mill for 6 hours (30 min at a time spaced by 30 min intervals) with zirconium oxide balls. The grinding was performed in suspension with ethanol in a ratio of 1:1. At the end of the grinding, it was dried again at 60 ºC to evaporate the ethanol. To obtain the powder, it was ground again, but this time with a mortar and pestle, and the result is shown in Figure 1(c).

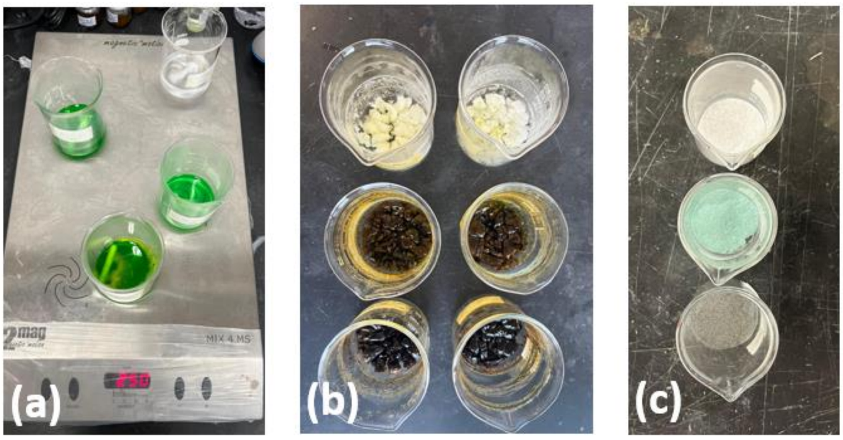

Figure 1 - (a) Synthesis of mesoporous bioactive glass (MBG) using the EISA process, showing the initial gel formation. (b) Calcined MBG samples after heat treatment. (c) Final ground MBG powders obtained through grinding with a mortar and pestle.

Table 1- Molar Ratios and Amounts of Reactants of the MBG

sample name	Molar Ratio Cu/Ca/P/Si	$CuCl_2$ (g)	$Ca(NO_3)_2$ (g)	TEP (mL)	TEOS (mL)
BG0	0/15/5/80	0	4.25	2.04	21.44
BG2	2/13/5/80	0.41	3.68	2.04	21.44
BG5	5/10/5/80	1.02	2.83	2.04	21.44

All the synthesis were carried out with 8 g of P123, 120 mL of ethanol, and 1.68 mL of HCl (0.5 M).

3.2 Synthesis of SPIONs deposited on mesoporous bioactive glass (SPIONs@MBG)

The SDBGs were prepared using the methods described in a previous procedure [19],[6]. Briefly, to prepare a sample of SDBG, designated BG0S, 1 g of sample BG0 was dispersed in 100 mL of pure water using an ultrasonic bath for 15 minutes. This solution was transferred to a 250 mL three-necked round bottom flask containing a ferric chloride solution with 2.5 mmol (0.50 g) $FeCl_2 \cdot 4H_2O$ and 5 mmol (1.35 g) $FeCl_3 \cdot {}_6H_2O$. After dissolution by stirring at 500 rpm, the solution was then degassed by bubbling with N_2 for 5 minutes. After sealing the system, 10 mL of a 25% aqueous ammonium solution was quickly added, which was indicated by a color change to black. After 5 minutes of reaction, 50 mL of ultrapure water was added to stop the reaction. The solution was transferred to a Falcon tube and washed 5 times with water using a magnet and a pipette. It was dried at 60ºC for 4 to 7 days. The powder was grounded with a mortar and pestle. To obtain the samples designated BG2S and BG5S, the same procedure was followed, with the exception that 1 g of BG2 and 1 g of BG5 were dispersed in 100 mL of pure water, respectively, instead of 1 g of BG0.

3.3 Evaluation of bioactivity and biodegradation

Following the ISO 23317:2017 standard, the bioactivity of the BG0, BG2, and BG5 samples was evaluated by compressing the powdered materials into disk-shaped pellets, each with a diameter of 7 mm and a weight of 0.5 g. These pellets were then placed in separate flasks containing SBF and incubated at a constant temperature of 37°C for various time intervals, including 3, 8, 24, 48, and 72 hours, as well as 7 days. The protocol for SBF preparation is detailed in Appendix A.4. The volume of SBF needed for each sample was determined using a specific formula **Eq 1**:

$$V_s = 100MM \times S_a, \qquad \textbf{Eq.1}$$

where V_s is the volume of SBF in mm^3, and S_a is the surface area of the pellet in mm^2. Once the immersion period concluded, the pellets were taken out from the SBF medium, gently rinsed using deionized water, and then dried at 60ºC for 6 hours. The dried samples were subsequently analyzed using a scanning electron microscope (SEM) to observe the formation of the apatite layer, and the ion release into the biological solution was evaluated through inductively coupled plasma (ICP) analysis, using the TM3030Plus Tabletop Microscope.

3.4 Development of injectable cement

Injectable cements were developed by mixing the MBG powders (solid phase, S) with a liquid phase (L) composed of an ammonium phosphate buffer. Various compositions were produced by varying the L/S ratio. The rheological properties and setting times of these compositions were then evaluated and optimized to ensure suitable performance for the intended applications.

4

RESULTS AND DISCUSSION

In the following sections, the properties of the prepared MBG and SPIONs@MBG are analyzed, discussed, and compared with those reported in the literature.

4.1 Characterization

4.1.1 Particle Size Distribution of MBG Samples

The particle size distributions of BG0, BG2, and BG5 are shown in Figure 2. BG0 shows a narrow distribution with a median particle size (d(0.5)) of 2.324 µm, indicating a relatively uniform particle size. In contrast, BG2 has a broader distribution centered around 1.263 µm, indicating a more heterogeneous particle size range. BG5 has the widest distribution with a median size of 2.612 µm and a significant presence of larger particles as indicated by a d(0.9) value of 17.934 µm. This variability in particle size, particularly in BG5, could affect the physical and biological properties of the material.

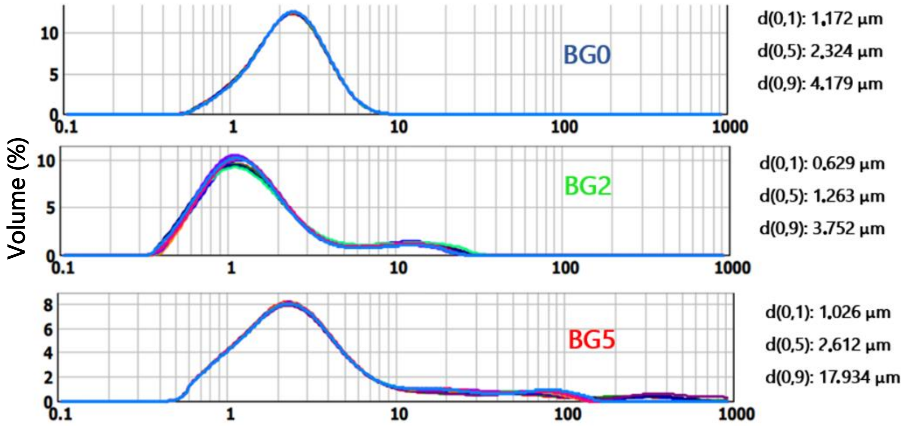

Figure 2 - Particle Size Distribution of BG0, BG2 and BG5.

4.1.2 Nitrogen Sorption Isotherms and Pore Structure

The nitrogen sorption isotherm of BG0 exhibits a type IV profile with H1 hysteresis loops, indicative of mesoporous materials with one-dimensional cylindrical channels [20], as observed in Figure 3(a) and 4(a). Additionally, Figure 3(b) shows an average pore diameter of approximately 4.81 nm. Similar nitrogen sorption isotherms were observed for BG2 and BG5, as detailed in Appendix A.4. Table 2 provides key data on the BET surface area, pore volume, and pore size of the MBG samples. The BET surface area varies significantly across the samples, with BG5 showing the highest value at 395.6 m^2/g, followed by BG0 with 260.8 m^2/g, and BG2 with 198.7 m^2/g. The increased surface area in BG5 indicates a greater extent of exposed surface for interactions, which is likely to enhance its reactivity and bioactivity. The pore volume follows a similar trend to the BET surface area, with BG5 having the largest pore volume at 0.39 cm^3/g. BG0 and BG2 have lower pore volumes at 0.31 cm^3/g and 0.21 cm^3/g, respectively. The average pore size shows a slight variation among the samples, with BG0 having the largest pore size at 4.81 nm, followed by BG2 at 4.56 nm, and BG5 with the smallest pore size at 3.97 nm [20].

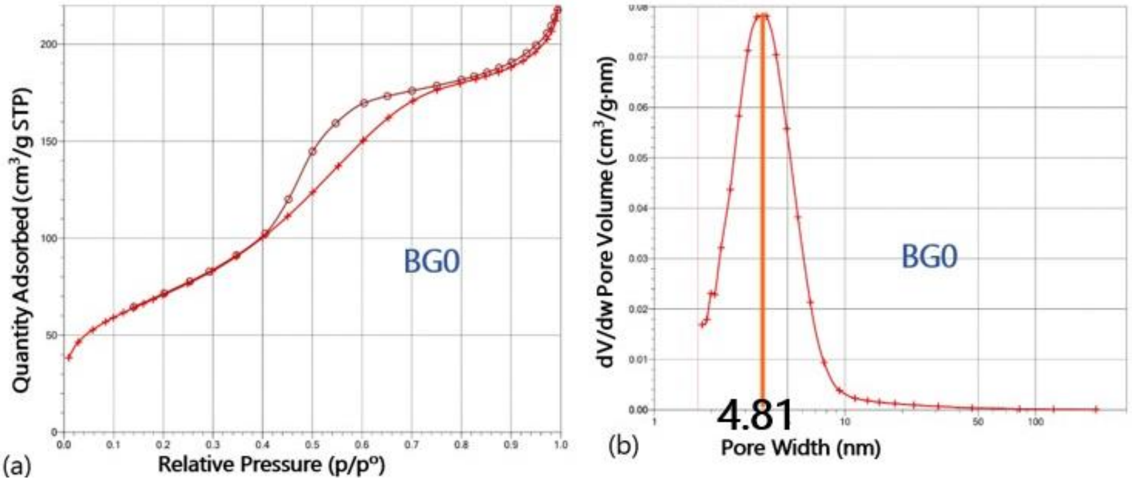

Figure 3 - (a) Isotherm Linear Plot of the sample BG0; (b) BJH Adsorption dV/dw Pore Volume of the sample BG0.

Table 2 - BET surface area, pore volume, and pore size of MBGs.

Sample	BET surface area [$m^2\ g^{-1}$]	Pore volume [$cm^3\ g^{-1}$]	Pore size [nm]
BG0	260.8	0.31	4.81
BG2	198.7	0.21	4.56
BG5	395.6	0.39	3.97

4.1.3 Structural Analysis via Electron Microscopy

The Scanning Transmission Electron Microscopy (STEM) image of the BG0 sample reveals a highly ordered periodic arrangement of pores, with the mesoporous structure remaining intact, as shown in Figure 4(a) [21]. STEM analysis of the BG2 sample, which exhibits similar characteristics to BG0, also shows a periodic arrangement of pores, as demonstrated in Figure A5 provided in Appendix A.5. The second STEM image (Figure 4(b)), taken at a 2 nm scale from the BG5 sample, reveals a periodic arrangement of pores with remarkable clarity and detail [21].

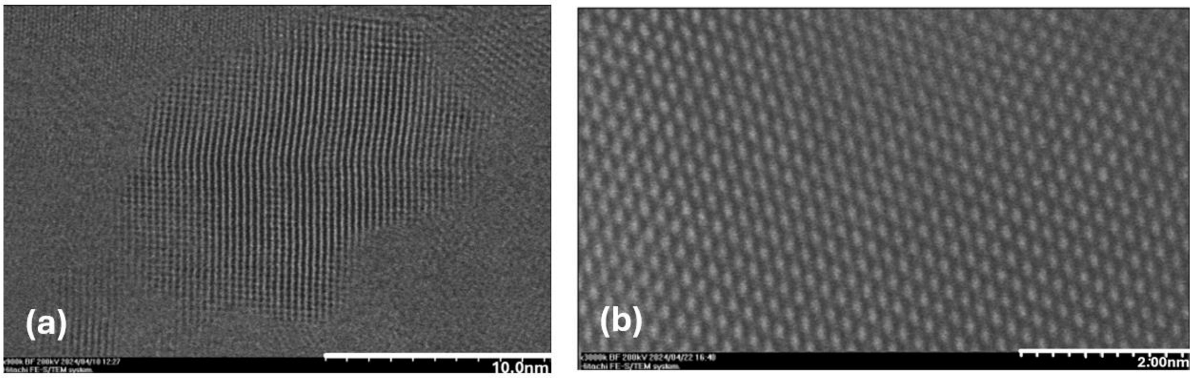

Figure 4 - (a) STEM Image obtained from the BG0 sample; (b) STEM Image obtained from the BG5 sample.

4.1.4 Effect of SPIONs Incorporation on Particle Size Distribution

The particle size distribution analysis of BG0S, BG2S, and BG5S (Figure 5) reveals that copper doping and the introduction of SPIONs have a significant impact on controlling particle size within mesoporous bioactive glass. The undoped BG0S sample exhibits the broadest distribution with larger particle sizes, indicating less control over particle formation. When compared to the particle size distribution of the MBG samples (BG0, BG2, BG5), it is evident that the presence of SPIONs plays a crucial role in redefining particle size. Notably, after incorporating SPIONs, the powder was not subjected to ball milling again, which may have contributed to the observed heterogeneity. This highlights the potential impact of additional processing steps in achieving a more uniform particle size distribution.

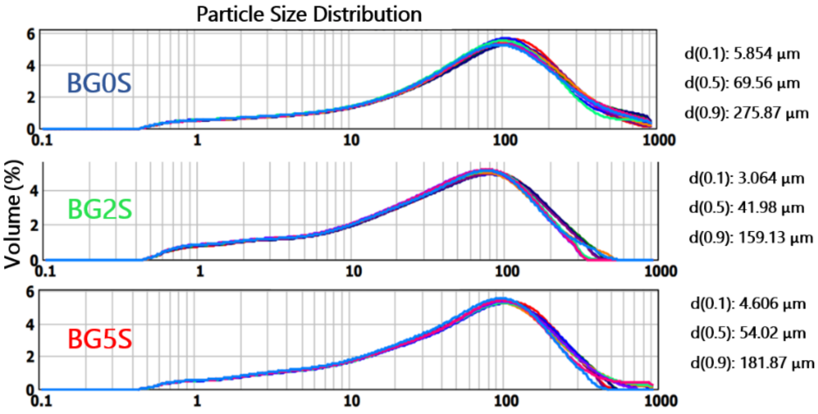

Figure 5 - Particle Size Distribution of BG0S, BG2S and BG5S.

4.1.5 FTIR and XRD Analysis of MBG and SPIONs@MBG

In the Fourier-transform infrared spectroscopy (FTIR) spectra (figure 6(a)) of the synthesized MBGs, the prominent bands around 455-470 cm^{-1}, 800 cm^{-1}, and 1070 cm^{-1} are characteristic of the Si–O–Si bending, symmetric stretching, and asymmetric stretching vibrations, respectively. In addition, the weak absorption band at 1238 cm^{-1} is associated with the presence of PO_4^{3-} groups in the glass matrix, and it does not indicate the formation of an apatite-like phase [22].

Regarding the XRD analysis (figure 6(b)), all patterns exhibit a broad band at approximately 22°, indicative of the amorphous silicate structure characteristic of bioactive glasses. In the BG2 and BG5 samples, two additional diffraction peaks are observed at 35° and 38°, corresponding to the (002) and (111) crystal planes of CuO (JCPDS 48-1548), respectively, consistent with findings reported by Li *et al.* [23]. Notably, these peaks are much weaker in BG2 compared to BG5. As the copper concentration increases from BG0 to BG5, more distinct crystalline peaks emerge at 21.50°, 27.37°, 31.54°, 35.52°, and 38.72° in the BG5 pattern. It was found that the crystallite size increased with copper doping due to particle clustering [24].

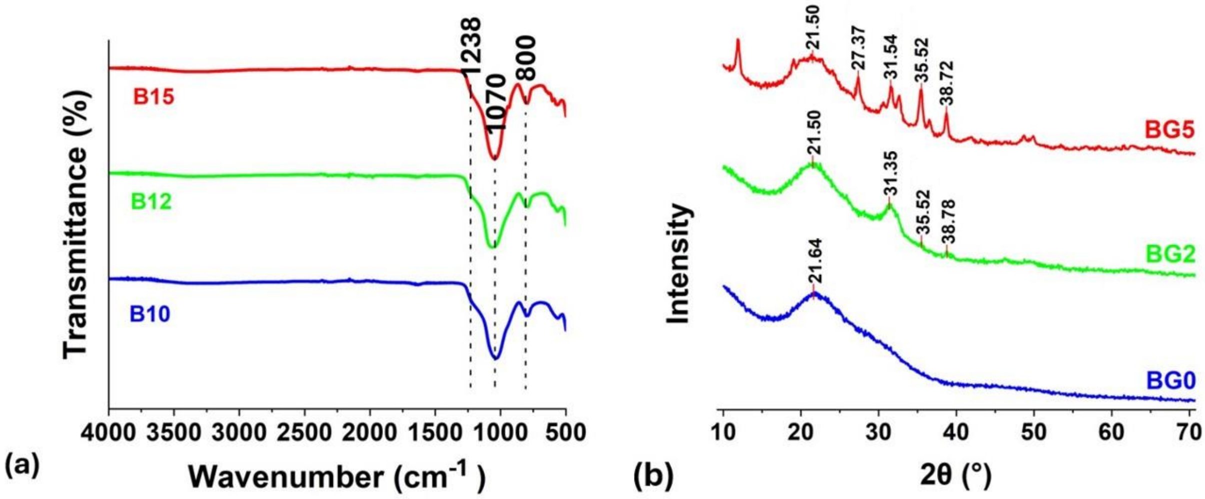

Figure 6 - (a) FTIR spectra of BG0, BG2, and BG5; (b) XRD patterns of BG0, BG2, and BG5.

The FTIR spectra in Figure 7(a) reveal that all SPIONs@MBG samples exhibit characteristic Si–O–Si bands at 800 and 1000–1200 cm^{-1}, indicating that the silicate network remains intact. A weak Fe–O band observed at 570 cm^{-1} in all samples indicates the incorporation of iron oxide. This band can be attributed to the Fe–O stretching vibrations in both tetrahedral and octahedral sites of Fe_3O_4 particles. Additionally, the frequency shoulder near 600 cm^{-1} suggests a similar vibration in γ-Fe_2O_3 or a defective spinel phase closely related to it [25]. The bands observed around 1649 cm^{-1} correspond to the bending vibration modes of water (O−H) groups. Additionally, the absorption bands near 3432 cm^{-1} are associated with −OH groups, indicating the presence of silanol groups on the surface of the glass [22]. This suggests that SPIONs contribute to increased surface hydration. These results highlight the successful integration of SPIONs, preserving the glass structure while introducing iron oxide and increasing surface activity.

The XRD patterns shown in Figure 7(b) for BG0S, BG2S, and BG5S samples show peaks aligned with the characteristic planes of magnetite (Fe_3O_4), confirming the successful incorporation of SPIONs into the BG matrix. The most prominent peaks are observed at approximately 31.8°, 32.3°, 31.9°, 61.5°, 61.0° and 60.6°, corresponding to the 220 and 440 planes of magnetite (Fe_3O_4) [26]. In addition to these characteristic reflections of magnetite, the samples show a broad hump between 20° and 25°, especially in the BG0S sample, which is indicative of the amorphous nature of the BG matrix. This broad feature suggests that the glass retains its amorphous structure, while the presence of crystalline peaks associated with SPIONs confirms the successful formation of a composite material [19].

The slight shift observed in the XRD peaks for the SPIONs@MBG samples occurs throughout the pattern and could be related to the insufficient initial dispersion of the oxides within the BG matrix, leading to inconsistencies in the homogeneity of the sample. Moreover, the coprecipitation method used to synthesize SPIONs can also influence the XRD results. Producing monodisperse, pure magnetite using this method can be challenging, and the resulting product may contain both magnetite (Fe_3O_4) and maghemite (y-Fe_2O_3). However, considering the color of the final product—magnetite being typically brownish-black and maghemite reddish-brown—and the XRD data (as shown in Figure 7(b)), it is determined that the synthesized material primarily consists of SPIONs with a magnetite core (Fe_3O_4). Additionally, the broad diffraction peaks indicate that the particles are in the nanometer size range, characteristic of superparamagnetic nanoparticles [26].

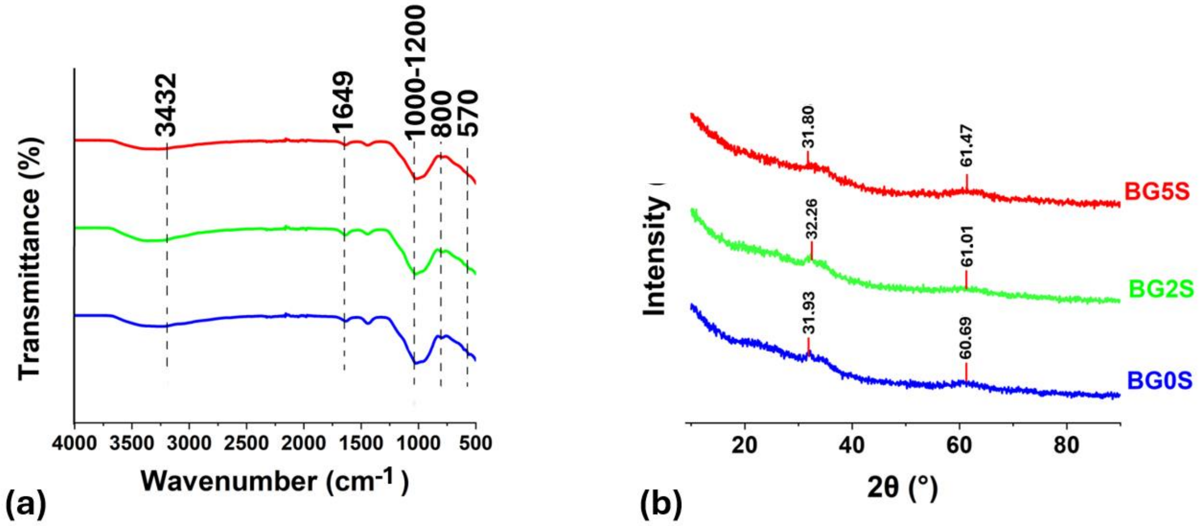

Figure 7 - (a) FTIR spectra of BG0S, BG2S, and BG5S; (b) XRD patterns of BG0S, BG2S, and BG5S.

4.1.6 SQUID Analysis of SPIONs@MBG

The magnetic behavior of the non-doped SPIONs@MBG sample was characterized at 300 kelvin and 10 kelvin, revealing distinct differences in response. These results can be compared with the findings of Cansu Taşar *et al.*, who analyzed SDBG nanoparticles [19].
As shown in Figure 8(a), at 300 K, the SPIONs@MBG sample exhibits a linear increase in magnetization, consistent with the behavior of a paramagnetic material. In contrast, as shown in Figure 8(b), at 10 K, the SPIONs@MBG sample displays a nonlinear, S-shaped curve, typical of superparamagnetic materials [27]. At this temperature, the magnetization reaches approximately 9 emu/g, a value similar to the SDBG sample at 300 K in Taşar *et al.*'s study.

When comparing the two results, the higher magnetization observed in the SDBG sample at 10K can be explained by the surface-deposited SPIONs, which interact more directly with the applied magnetic field. In contrast, the lower magnetization in the SPIONs@MBG sample at 300 K may be attributed to the particles being more dispersed within the matrix, reducing their collective magnetic response. At 10 K, the reduced thermal agitation allows the SPIONs in the matrix to align more efficiently with the magnetic field, leading to magnetization levels similar to those observed in the SDBG sample at room temperature in Taşar *et al.*'s study. The temperature-dependent magnetic behavior of SPIONs@MBG is crucial for applications like magnetic hyperthermia. This highlights the importance of understanding the relationship between SPION distribution and temperature in the design of materials for specific magnetic applications.

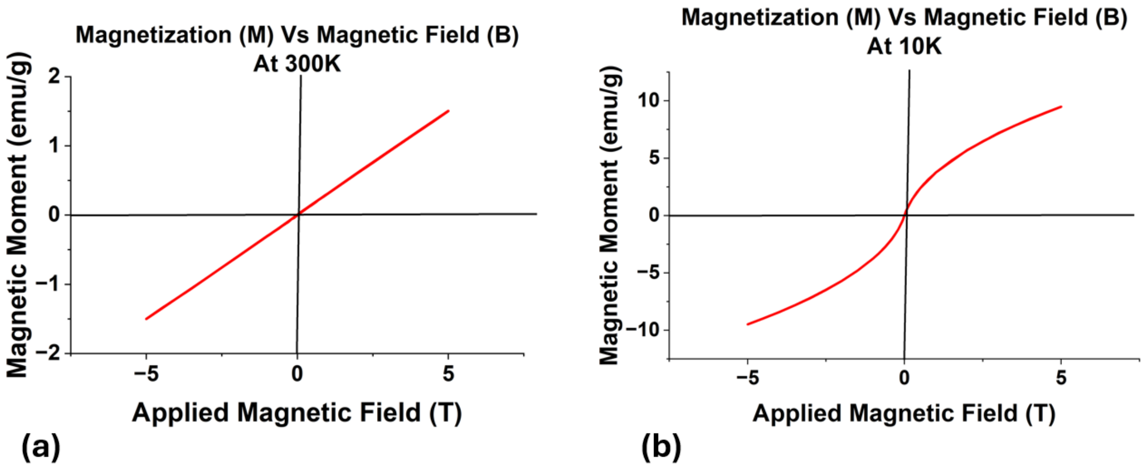

Figure 8 - Magnetization (*M*) versus Applied Magnetic Field (*B*) curves for the non-doped SPIONs@MBG at two different temperatures.

4.2 Evaluation of bioactivity and biodegradation

The formation of hydroxyapatite (HA) in BG samples was evaluated by calculating the calcium-to-phosphorus (Ca/P) ratio, determined using energy-dispersive X-ray spectroscopy (EDS). The elemental composition data used for these calculations is provided in Figure A6 found in section A.6 of the Appendix. HA, the mineral phase typically formed on bioactive materials when immersed in SBF, has a stoichiometric Ca/P ratio of approximately 1.67. A ratio close to this value indicates the formation of stoichiometric hydroxyapatite, which is crucial for assessing the bioactivity of the material. Deviations from this ideal ratio can suggest either incomplete hydroxyapatite formation or the presence of other calcium-rich phases [5].

BG0:

- **3 h**: The SEM image in Figure 9 shows a rough, granular surface with little to no distinct spherical structures, corresponding to a high Ca/P ratio of 2.24, indicating limited hydroxyapatite formation.
- **24 h**: The surface is more defined with noticeable clusters of spherical particles, likely indicative of hydroxyapatite. The Ca/P ratio drops to 1.77, aligning closely with stoichiometric hydroxyapatite.
- **72 h**: A well-developed layer of spherical structures is visible, suggesting significant apatite formation. The Ca/P ratio further decreases to 1.59, confirming sustained hydroxyapatite growth.
- **7 days**: The surface appears less organized, and the Ca/P ratio increases to 2.56, possibly indicating excess calcium deposition or phase changes within the formed apatite layer.

BG2:

- **3 h**: The SEM image shows a rough surface with scattered small particles. The Ca/P ratio at this point is very high (7.37), suggesting an excess of calcium or poor hydroxyapatite formation at this early stage.
- **24 h**: More defined clusters of spherical particles appear, suggesting the initiation of hydroxyapatite formation. The Ca/P ratio decreases to 2.19, indicating a shift toward hydroxyapatite growth.
- **72 h**: The surface shows more extensive coverage by spherical particles, and the Ca/P ratio of 1.93 reflects continued hydroxyapatite formation, though slightly calcium rich.
- **7 days**: The surface appears more consolidated, with fewer distinct spheres, and the Ca/P ratio stabilizes at 1.64, indicating the formation of hydroxyapatite close to its stoichiometric ratio.

BG5:

- **3 h**: The SEM image shows a less organized surface with small, dispersed particles. The Ca/P ratio is 1.24, suggesting minimal hydroxyapatite formation.
- **24 h**: The surface shows more clusters of particles, with a Ca/P ratio of 1.77, indicating significant hydroxyapatite formation similar to BG0.
- **72 h**: The surface continues to show substantial apatite-like structures, and the Ca/P ratio remains stable at 1.22, though slightly lower than expected for pure hydroxyapatite.
- **7 days**: The SEM image reveals a more compact layer of spherical particles, and the Ca/P ratio remains near 1.75, confirming hydroxyapatite formation at a relatively stable rate, though copper might still be influencing the crystallization process.

The combined EDS and SEM analysis confirms that BG samples (BG0, BG2, and BG5) lead to the formation of hydroxyapatite upon immersion in SBF. BG0 showed a more consistent hydroxyapatite growth, particularly between 24h and 72h, with well-formed spherical apatite particles. BG2, doped with 2% copper, exhibited delayed hydroxyapatite formation but eventually reached a near-ideal Ca/P ratio after 7 days. BG5, with 5% copper, exhibited fluctuating Ca/P ratios and a less organized surface morphology at earlier time points, likely due to the inhibitory effect of higher copper content, but eventually demonstrated significant hydroxyapatite formation after 7 days.

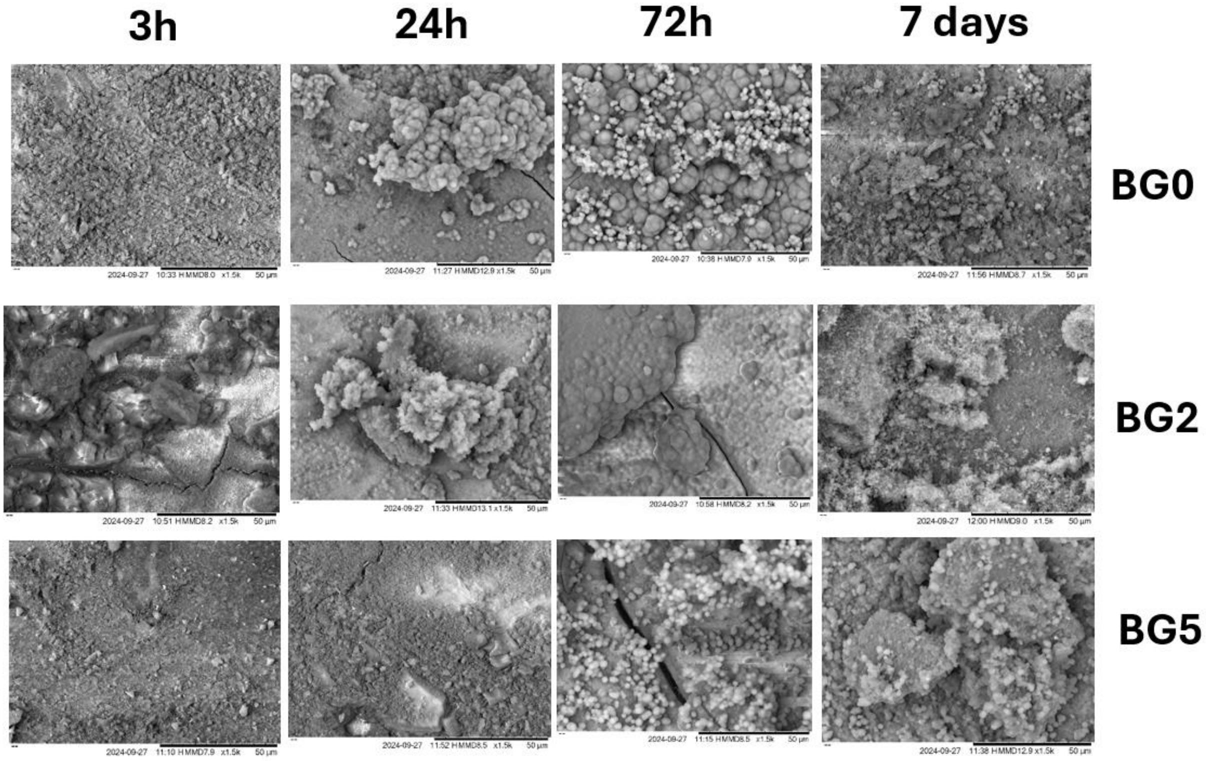

Figure 9 - SEM images of bioactive glass samples (BG0, BG2 and BG5) after immersion in simulated body fluid (SBF) for various time points: 3 hours, 24 hours, 72 hours, and 7 days. Magnification: x1.5k Scale bar: 50 µm.

The ICP analysis of BG0, BG2, and BG5 after immersion in SBF at 37ºC for 3 hours, 8 hours, 24 hours, 48 hours, 72 hours, and 7 days reveals significant differences in ion release behavior among the samples (Figure 10). This behavior is consistent with findings from other studies [28], which have shown that silicon is released at a relatively constant rate throughout the immersion period, while network-modifiers like Ca and Cu are preferentially released from the MBG network during the initial hours of immersion. Specifically, in similar composites, copper is rapidly released within the first 3 hours, reaching a concentration of approximately 9 mg/L in SBF, after which the release rate slows down, likely due to a change in the dissolution mechanism or the co-precipitation of Cu in HCA. In this study, a similar trend was observed, with copper concentrations increasing rapidly within the first 3 hours, reaching 7.94 mg/L for BG2 and 11.75 mg/L for BG5. This suggests that in BG2 and BG5, the controlled release of copper may be influenced by similar mechanisms after an initial rapid phase providing a sustained therapeutic effect in potential biomedical applications.

The initial increase in Ca concentration during immersion in SBF is due to the rapid dissolution of the bioactive glass, releasing Ca into the solution. However, as immersion progresses, both Ca and P concentrations decrease. This decrease occurs because these ions are consumed in the formation of HCA on the glass surface. HCA formation, which involves the incorporation of Ca and P from the SBF into a bone-like mineral layer, is a key indicator of the bioactivity of the glass [28].

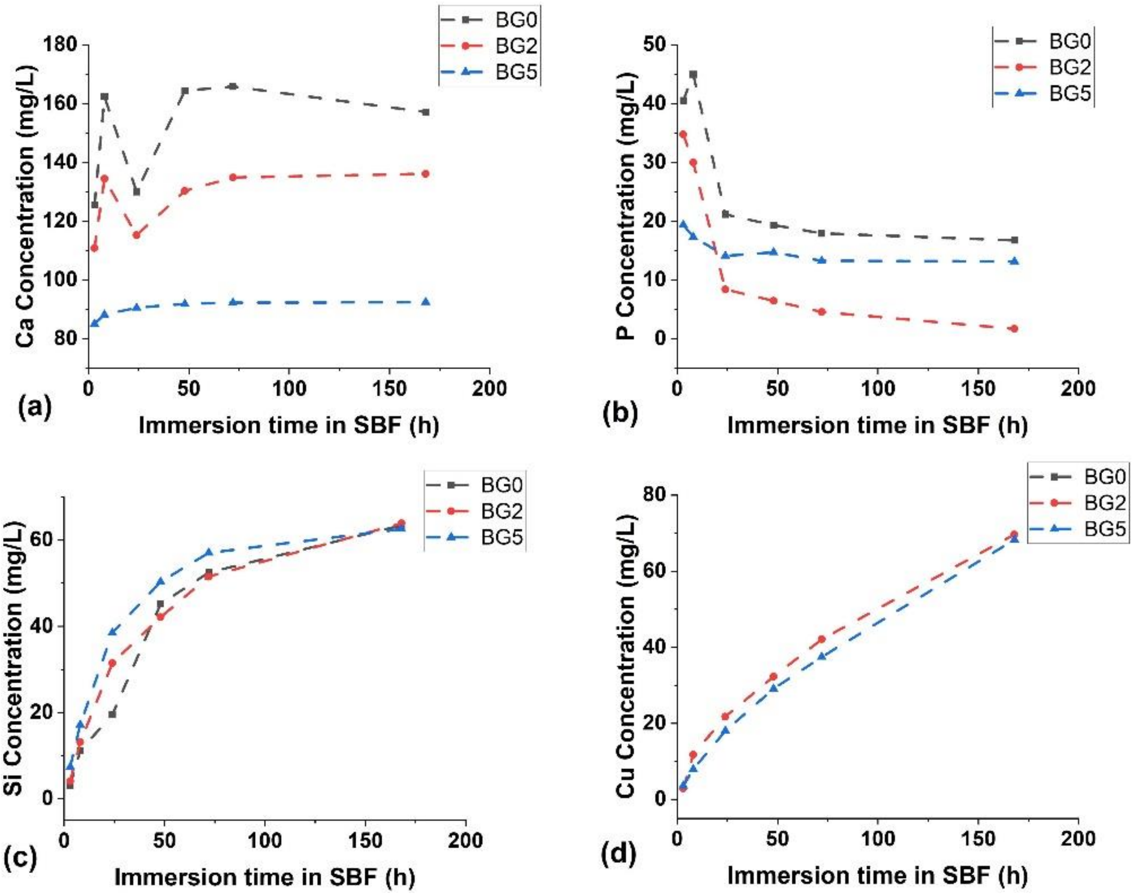

Figure 10 - ICP results for BG0, BG2, and BG5 after soaking in SBF solution: (a) Ca ion, (b) P ion, (c) Si ion, and (d) Cu ion.

4.3 Cytotoxicity Tests

Cell viability was assessed using a human osteosarcoma cell line (Saos-2), and the results are depicted in Figure 11. According to the ISO 10993-5 standard, cell viability greater than 70% indicates that the samples are non-cytotoxic. Furthermore, passivated versions of the MBGs and SPIONs@MBGs (BG0P, BG2P, BG5P, BG0SP, BG2SP, BG5SP) were analyzed to determine the effect of passivation on cytotoxicity.

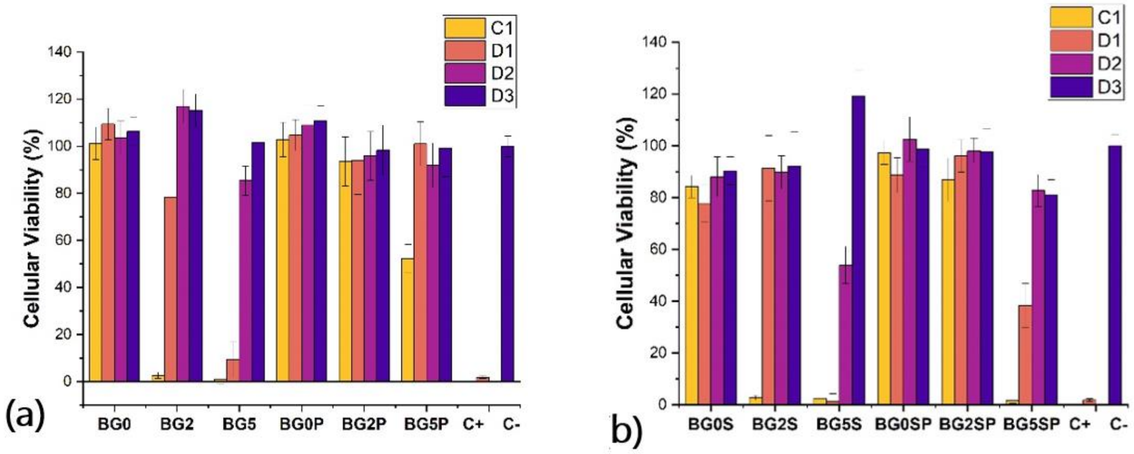

Figure 11 - Results of Saos-2 cells' viability obtained for the MBGs (a) and SPIONs@MBGs (b) C1 – initial concentration, D1 – first dilution; D2 – second dilution; D3 – third dilution; D4 - fourth dilution

The comparison between the two graphs (figure 11(a) and figure 11(b)) reveals the impact of incorporating SPIONs into MBGs, both in their passivated and non-passivated forms, on cellular viability.

1. **Non-Passivated Bioglasses (BG0, BG2, BG5 vs. BG0S, BG2S, BG5S)**:

In figure 11(a), which represents the non-SPION-deposited bioglasses, BG0 shows consistently high cell viability across all conditions, indicating good biocompatibility. In contrast, BG2 and BG5 exhibit significantly lower viability, especially in the C1 and D1 conditions, where they are severely cytotoxic. In figure 11(b), after the incorporation of SPIONs, BG0S maintains high cell viability similar to BG0. However, the incorporation of SPIONs in BG2S and BG5S shows a slight improvement in viability under certain conditions compared to their non-SPION counterparts (BG2 and BG5), although BG2S still exhibits severe cytotoxicity in C1, and BG5S follows the same trend in both C1 and D1

2. **Passivated Bioglasses (BG0P, BG2P, BG5P vs. BG0SP, BG2SP, BG5SP)**:

The passivated bioglasses in figure 11(a) (BG0P, BG2P, BG5P) generally show improved cell viability across most conditions compared to their non-passivated counterparts, with BG0P and BG2P maintaining high viability above 90% in all conditions. BG5P, however, maintains cell viability above 70% in all conditions except for C1, where it drops to around 50%, making it moderately cytotoxic. In figure 11(b), after SPION incorporation, BG0SP and BG2SP continue to exhibit high cell viability, similar to their counterparts without SPIONs, suggesting that the passivation effectively preserves biocompatibility even with SPIONs. BG5SP, despite being passivated, still demonstrates lower viability, particularly in the C1 condition.

The incorporation of SPIONs in bioglasses has a differential impact depending on the copper concentration. In lower copper-doped bioglasses (BG0S and BG2S), the addition of

SPIONs appears to have a minimal effect on biocompatibility, as these samples maintain similar or slightly improved cell viability compared to the non-SPION-deposited counterparts. However, in bioglasses with higher copper concentrations (BG5S and BG5SP), the incorporation of SPIONs does not fully mitigate the cytotoxic effects. Although there is a slight improvement in cell viability in some conditions, the overall cytotoxicity remains significant, suggesting that SPIONs do not entirely overcome the biocompatibility challenges associated with high copper content.

4.4 Antibacterial activity

The antibacterial activity of the doped MBG extracts against *Staphylococcus aureus* (S. aureus) and *Escherichia coli* (E. coli) was evaluated according to ISO 20776-1 guidelines to determine the Minimum Inhibitory Concentration (MIC). The results were based on the presence or absence of bacterial growth on the agar plates, as presented in Figure 12.

In Figure 12(a), which illustrates the antibacterial activity against *S. aureus*, BG2 at 100% extract concentration (positions 2 and 3) was not fully effective, as bacterial colonies remained visible. Conversely, BG5 at 100% concentration (positions 5 and 7) successfully eliminated *S. aureus*, indicated by the absence of bacterial colonies, demonstrating its potent antibacterial effect. However, when the concentration of BG5 was reduced to 50% (positions 10 and 11), bacterial colonies reappeared, indicating a reduced antibacterial efficacy at lower concentrations. Additionally, BG5P at 100% concentration (positions 14 and 15) also failed to completely eliminate *S. aureus*, suggesting that passivation reduces the antibacterial potency of BG5.

For *E. coli*, Figure 12(b) shows that BG2 at 100% concentration (positions 2 and 3) was similarly ineffective, as bacterial colonies were observed. In contrast, BG5 at 100% concentration (position 14) demonstrated strong antibacterial properties, with no bacterial growth. However, at position 15, which also represents BG5 at 100%, bacterial colonies were still visible, indicating some inconsistency in BG5's antibacterial performance against *E. coli*.

When compared to literature, these results align with previous findings. Studies have shown that copper-doped bioactive glasses exhibit significant antibacterial activity against both *S. aureus* and *E. coli* at lower concentrations. For example, Bari *et al.* reported that copper-doped MBGs demonstrated effective antibacterial action with MIC values as low as 2 mg/mL to 10 mg/mL for *E. coli* and *S. aureus* [29]. Additionally, other studies indicate MIC values of 25 mg/mL and MBC (Minimum Bactericidal Concentration) of 50 mg/mL for similar bioactive glasses against *E. coli* [29]. In this study, the concentration of 100 mg/mL was significantly higher than those typically reported in the literature. Although BG5 was effective at 100% concentration, the observed efficacy decrease at 50% concentration suggests that a higher concentration may be required for this specific formulation compared to other copper-doped bioactive glasses.

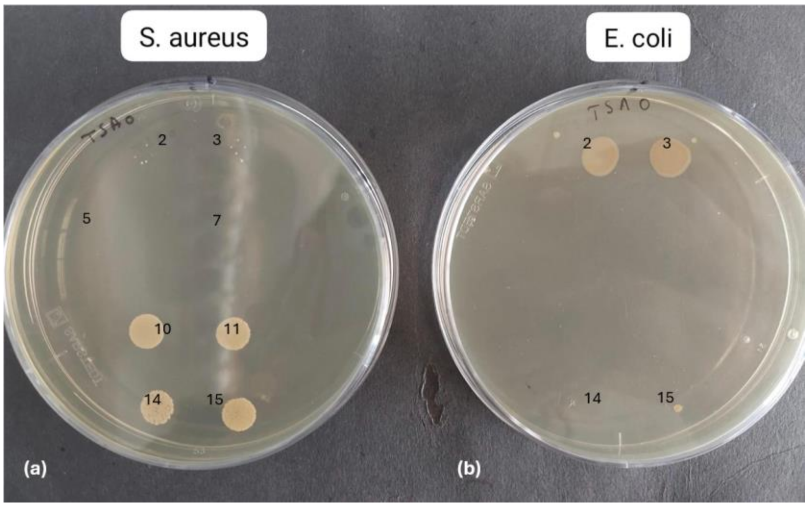

Figure 12 - Antibacterial activity of various MBG samples against **(a)** *Staphylococcus aureus* and **(b)** *Escherichia coli*. The agar plates show the effects of different concentrations and types of MBG extracts (BG2, BG5, BG5P) on bacterial growth, indicating varying degrees of inhibition. The absence or presence of bacterial colonies provides a visual representation of the effectiveness of each sample in eliminating or reducing bacterial growth.

In the case of the SPIONs@MBG samples, the wells in the microdilution assay appeared opaque (Figure 13), indicating that bacterial growth occurred despite the presence of the SPIONs@MBG extracts. Opaqueness in the wells is typically a sign that the bacteria were able to proliferate, which suggests that the extracts were not sufficiently effective at inhibiting or killing the bacteria. This result implies that the antibacterial properties of the SPIONs@MBG were not strong enough to prevent bacterial growth under the tested conditions. Consequently, these extracts were not applied to agar plates as the initial microdilution assay already demonstrated a lack of efficacy. The opaqueness observed in the wells serves as a clear indicator that the SPIONs@MBG did not provide the desired antibacterial effect in this instance, highlighting the need for further optimization of the material's composition or concentration to enhance its antibacterial activity.

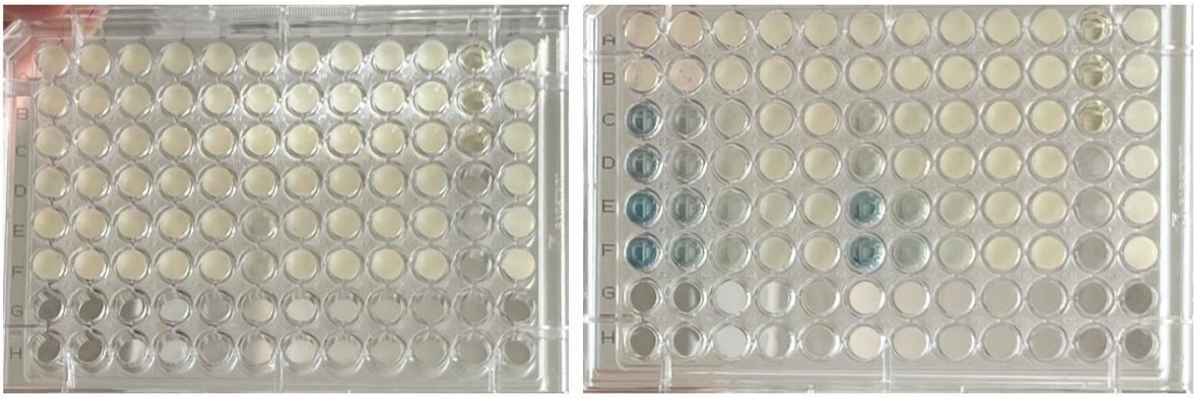

Figure 13 - Comparison of two microdilution assay plates. The left plate shows opaque wells for SPIONs@MBG samples, indicating bacterial growth across all tested conditions, suggesting that the extracts were not effective in inhibiting bacterial proliferation. In contrast, the right plate is used as a comparison, where some wells show a clear change in color (blue), indicating successful inhibition of bacterial growth in those specific wells.

The antibacterial effects of SPIONs are primarily linked to their ability to generate reactive oxygen species (ROS) and physically interact with bacterial membranes, contributing to cell damage and death. Recent studies, such as Gholami *et al.* (2020), have demonstrated that SPIONs exhibit significant antibacterial activity under both aerobic and anaerobic conditions by promoting oxidative stress and inducing ROS formation [30]. In this study, the antibacterial activity of copper ions was shown to decrease when SPIONs were added to the system. This may be due to the "masking" effect of SPIONs, as they compete with copper for ROS generation. The physical interaction between SPIONs and bacterial membranes, along with the iron ions released from the SPIONs, could interfere with the release and effectiveness of copper ions in the composite, thereby reducing their bactericidal efficiency [30].

4.5 Rheological properties of cements

In the development of injectable bone cements, the optimization of rheological properties is crucial to ensure proper handling, injectability, and *in situ* setting behavior. However, achieving the right balance between fluidity for easy injection and rapid setting for mechanical stability remains a challenge. The liquid-to-solid (L/S) ratio is a key parameter that influences the rheological behavior and setting time of the cement. A higher L/S ratio generally results in a more fluid mixture, which may be easier to inject but can lead to prolonged setting times and inadequate mechanical properties. Conversely, a lower L/S ratio typically produces a stiffer, faster-setting cement, but it may compromise injectability [31].

In this study, we investigated the effects of different L/S ratios on the rheological properties and setting behavior of MBG-based cements. Initial tests with L/S ratios of 2 and 2.5 revealed that these compositions were too fluid, exhibiting excessively long setting times. Therefore, the focus was shifted to L/S ratios of 1.50 and 1.75, which offered a better balance between fluidity and setting time. The storage modulus (G') was measured as a function of time to assess the setting process of the cements at these ratios. This modulus provides a direct measure of the material's stiffness as it transitions from a liquid to a solid state. The results, presented in Figure 14, offer insights into the optimal L/S ratio for achieving the desired rheological and mechanical properties in MBG-based injectable bone cements.

Figure 14 presents the evolution of the storage modulus (G') over time at a frequency of 1 Hz and a temperature of 37°C for different MBG compositions (BG0, BG2, and BG5) with L/S ratios of 1.50 and 1.75. The storage modulus (G') is an important indicator of the material's stiffness and offers valuable insights into the setting behavior of the cement.

For all compositions (BG0, BG2, and BG5), the storage modulus (G') increases steadily over time, reflecting the progression of the setting reaction as the material transitions from a more fluid-like state to a solid-like state.

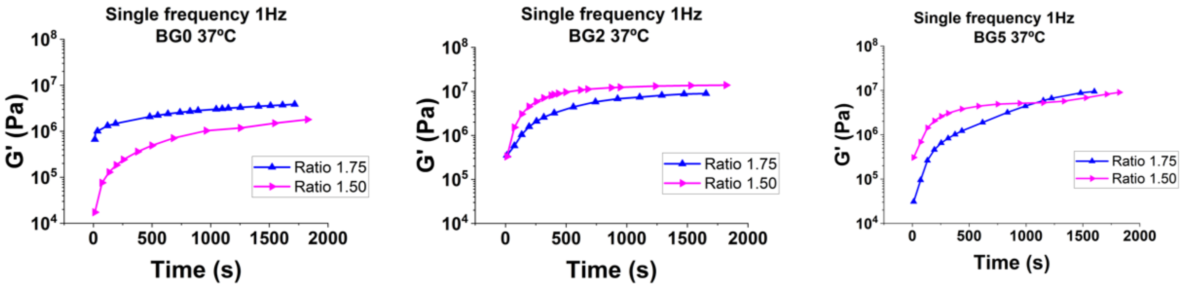

Figure 14 - Evolution of the storage modulus (G') over time at 1 Hz and 37°C for MBG cements (BG0, BG2, BG5) with liquid-to-solid (L/S) ratios of 1.50 and 1.75.

- **BG0**: In the first graph of Figure 14, BG0 shows a clear increase in G' for both L/S ratios. The L/S ratio of 1.50 results in a more rapid increase in stiffness, indicating that this ratio accelerates the setting process and leads to a firmer material more quickly.
- **BG2**: The second graph for BG2 also demonstrates an increasing trend in G', with the L/S ratio of 1.50 again reaching higher modulus values at a faster rate compared to the L/S ratio of 1.75. This suggests that the BG2 behaves similarly to BG0, where a lower L/S ratio promotes faster setting and greater stiffness.

- **BG5**: The third graph for BG5 shows a consistent trend of increasing storage modulus over time. The L/S ratio of 1.50 shows a steeper increase in G', indicating a faster and more pronounced setting process compared to the L/S ratio of 1.75.

The S-curve shape observed in these graphs, characterized by a rapid increase in modulus followed by a plateau, indicates that the setting reaction reaches a steady state. This plateau represents the completion of the setting reaction, where the material achieves its final mechanical properties. As mentioned in related literature [32], the doubling of the modulus at the plateau signifies that the cement has fully set and has reached its intended stiffness.

Overall, the data from Figure 14 indicate that the L/S ratio has a significant impact on the setting time and final stiffness of the MBG cements. Lower L/S ratios, specifically 1.50, consistently lead to faster setting and higher stiffness across all compositions tested. These findings are critical for optimizing the rheological properties of injectable cements, ensuring they meet the necessary criteria for specific clinical applications, where setting time and mechanical strength are key parameters [31].

4.5.1 Impact of SPIONs@MBG on the Rheological Properties of MBG Cements

For the SPION@MBG cements, a L/S ratio of 1:1 was used, as shown in Figure 15. This ratio was chosen because higher L/S ratios of 1.75 and 1.50 resulted in mixtures that were too fluid, making the cements impractical due to their excessively liquid consistency.

- **SPIONs@MBG0**: Compared to its non-SPION counterpart, SPIONs@MBG0 shows a much slower increase in G', with the final modulus reaching only about 10^4 Pa. This suggests that the addition of SPIONs significantly reduces the stiffness of the cement, and the material remains relatively soft throughout the setting process.
- **SPIONs@MBG2**: SPIONs@MBG2 exhibits a more pronounced increase in G' compared to SPIONs@MBG0, with a final modulus around 10^5 Pa. However, this is still lower than the non-SPION version of BG2, indicating that while SPIONs enhance the stiffness compared to SPIONs@MBG0, they still reduce the overall stiffness compared to BG2.
- **SPIONs@MBG5**: SPIONs@MBG5 shows the highest initial modulus among the SPION-deposited cements, with a final value reaching 10^6 Pa. However, the curve suggests that the setting process was likely captured late, as the typical initial rise in modulus is not observed. Despite this, the final stiffness of SPIONs@MBG5 is comparable to that of BG5,

indicating that the addition of SPIONs, in this case, does not significantly compromise the final rheological properties.

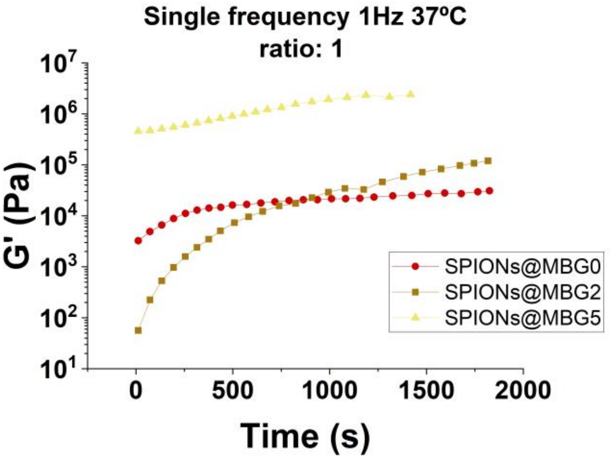

Figure 15 - Evolution of the storage modulus (G') over time at 1 Hz and 37°C for SPION-deposited MBG cements (SPIONs@MBG0, SPIONs@MBG2, SPIONs@MBG5) with a liquid-to-solid (L/S) ratio of 1:1.

Comparison between the non-SPION and SPIONs@MBG cements reveals that the presence of SPIONs generally slows down the setting process and reduces the final stiffness of the cements, as indicated by lower G' values for SPIONs@MBG0 and SPIONs@MBG2. However, in the case of SPIONs@MBG5, the final stiffness is comparable to that of the non-SPION BG5, suggesting that the higher copper content in BG5 may counteract the softening effect of SPIONs. The results also highlight the importance of the L/S ratio in determining the setting behavior and final properties of the cements. While lower L/S ratios typically lead to faster setting times and higher final stiffness, in the case of SPION-deposited samples, an L/S ratio of 1:1 was necessary to avoid overly liquid mixtures. This adjustment allowed for practical handling and measurement of the cements’ properties. Overall, the incorporation of SPIONs into MBG cements introduces complexity in the rheological behavior, particularly in how it interacts with different copper doping levels and L/S ratios. These findings suggest that while SPIONs can be beneficial for certain applications, their effects on the mechanical properties of the cement must be carefully considered and optimized based on the specific requirements of the intended use.

4.6 Evaluation of Setting Times for Bone Cements

In surgical bone regeneration procedures, the accurate placement of bone cement is crucial. Typically, a syringe is used to inject the cement paste into the repair site. The cement must have a setting time that allows the surgeon enough time to shape and position it properly, while also setting quickly enough to avoid washout or delaying wound closure. The initial setting time is important for shaping and filling, after which the cement should not be disturbed to avoid weakening the structure. Ideally, the final setting time should be as short as possible to minimize delays in wound closure, with recommended times being around 8 minutes for the initial setting and under 15 minutes for complete hardening, making it suitable for orthopedic applications [33].

For this study, the setting times of BG0, BG2, and BG5 bone cements were evaluated using a timer to measure the time taken for each sample to reach key stages in the setting process. The photographs provided in Figure 16 show the physical state of the samples during these tests. Among the tested compositions, BG2 demonstrated the most ideal behavior, aligning with the recommended setting times for orthopedic applications. At 8 minutes, BG2 remained extrudable through a syringe, corresponding to the first photo, and it fully solidified at 15 minutes, meeting the proposed guidelines. In comparison, BG5 exhibited slower setting characteristics. It only became extrudable at around 11 minutes and took approximately 20 minutes to fully harden. BG0, on the other hand, was notably slower, remaining extrudable for nearly 15 minutes before it finally solidified around the 30-minute mark.

From these observations, BG2, particularly with the liquid-to-solid (L/S) ratio of 1.5, is the most suitable composition for surgical use, as it meets the recommended setting times for initial syringe extrusion (8 minutes) and final hardening (15 minutes). BG5, while slower, may still be applicable with some adjustment to its composition. BG0, however, demonstrated an excessively long setting time, making it less ideal for use in situations where timely hardening is critical.

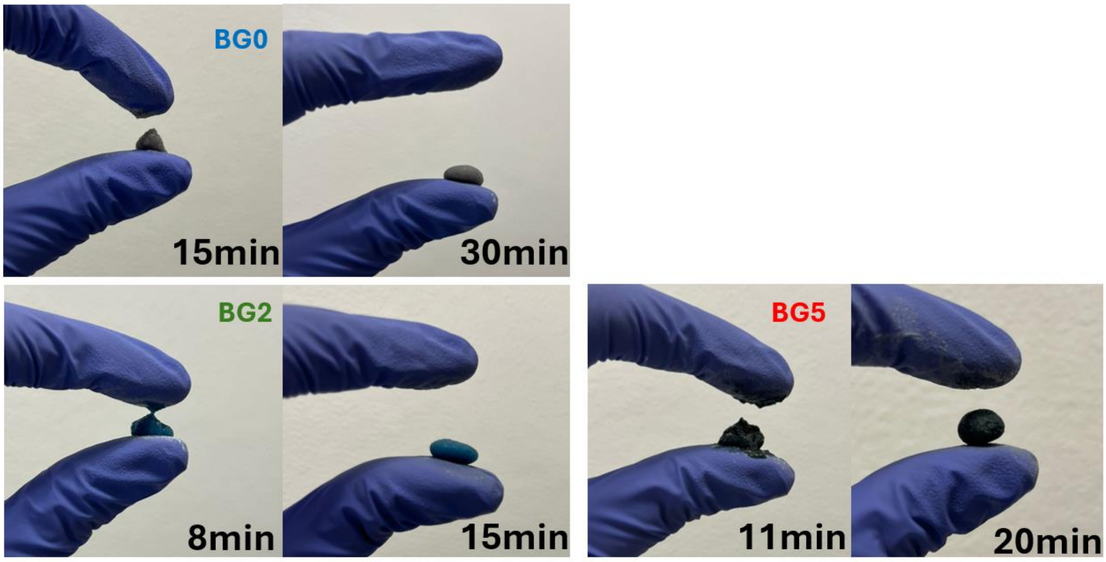

Figure 16 - Evaluation of the setting times of BG0, BG2, and BG5 bone cements for surgical bone regeneration applications.

4.7 Biological Activity of MBG-Based Cements

Figure 17 shows the antibacterial activity of the MBG-based cements against Gram-negative Escherichia coli (E. coli) (Figure 17(a)) and Gram-positive methicillin-resistant Staphylococcus aureus (MRSA) (Figure 17(b)). The Kirby-Bauer qualitative method was used to assess the antibacterial properties of the BG0, BG2, and BG5 samples. As mentioned in Appendix A.3, the MBG-based cements were prepared using an L/S ratio of 1.5.

Although some samples did not maintain a uniform shape and partially disintegrated in the medium, which may have affected the clarity of the results, all samples appeared to exhibit antibacterial activity, as suggested by the observed inhibition zones, though this cannot be confirmed with absolute certainty. Among the tested cements, BG5 exhibited the strongest antibacterial effect, particularly against MRSA, and was the only sample that did not disintegrate, while BG0 and BG2 demonstrated varying levels of activity. These results suggest that copper doping enhances the antibacterial effect, with higher copper concentrations being more effective, especially against Gram-positive bacteria [34]. Future tests with improved sample preparation are recommended to confirm these findings.

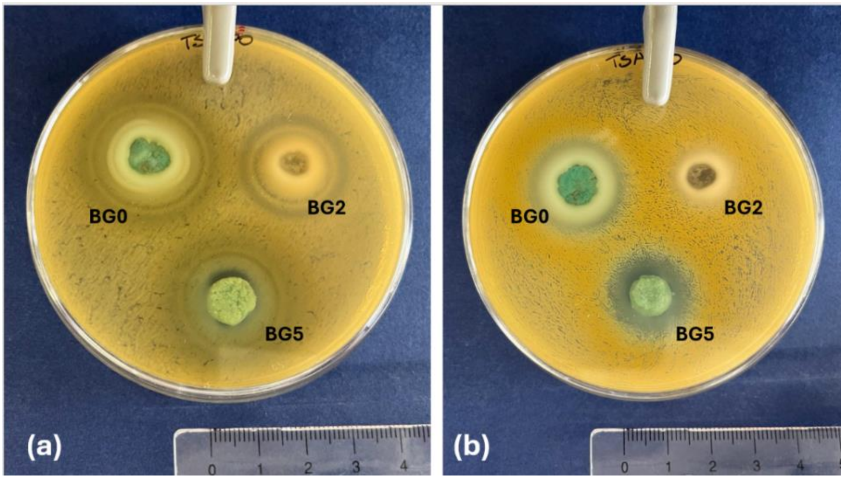

Figure 17 - Antibacterial activity of MBG-based cements against (a) Gram-negative Escherichia coli (E. coli) and (b) Gram-positive methicillin-resistant Staphylococcus aureus (MRSA), evaluated using the Kirby-Bauer method. The samples include BG0, BG2, and BG5. Inhibition zones around the samples indicate antibacterial activity.

4.8 Cytotoxicity Assessment of MBG-based cements

To evaluate the cytotoxicity of MBG-based cements, Saos-2 cells were cultured in McCoy's 5A medium, following the extract method as outlined in the ISO 10993-5 standard for in vitro cytotoxicity testing. The cement samples were prepared as seen in Figure A2 of the appendix. These samples were incubated in McCoy's 5A medium to prepare the extracts for cytotoxicity testing, as shown in Figure A1 of the appendix.

The results of the cellular viability were assessed through a resazurin assay. The Saos-2 cells were incubated with the extracts for 24 hours, and the results are illustrated in Figure 18 and Figure 19. Figure 18 clearly shows that BG0, BG2, and BG5 exhibit minimal cellular viability, as indicated by the low intensity across all conditions (C1, D1, D2, D3, D4, D5). In comparison, the positive control (C^+) showed high cellular viability, close to 100%. The negative control (C^-), as expected, demonstrated no viability. Since cell viability is well below 70% in all conditions for BG0, BG2, and BG5, according to the ISO 10993-5 standard, these samples can be classified as cytotoxic.

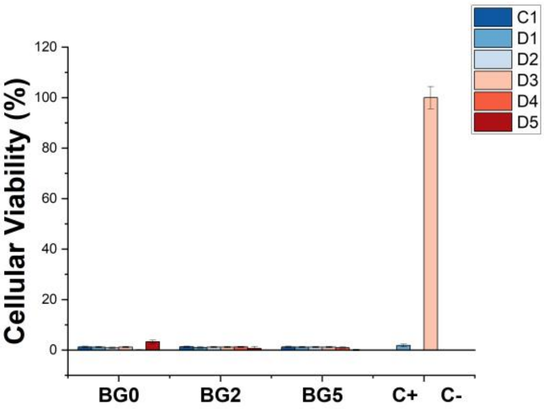

Figure 18 - Cellular viability results for Saos-2 cells exposed to extracts from MBG-based cements (BG0, BG2, and BG5) under different test conditions (C1 – initial concentration, D1 – first dilution; D2 – second dilution; D3 – third dilution; D4 - fourth dilution; D5 - fifth dilution)

Further confirmation of these results is visible in Figure 19, where the cytotoxicity of BG0, BG2, and BG5 can be observed visually through the resazurin color change. The Saos-2 cells showed minimal response when incubated with the extracts from MBG-based cements. Only the negative control (C^+) resulted in a significant color change, and the D5 dilution of BG0 appeared to show some potential viability. However, upon further examination of Figure 18, it becomes clear that BG0 remains cytotoxic. Meanwhile, the positive control (C^-) once again confirmed the absence of cellular activity, as expected.

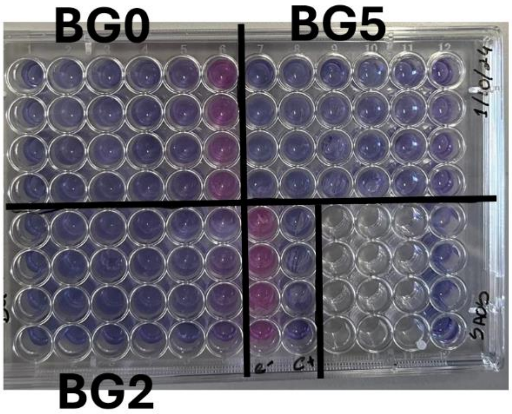

Figure 19 - Resazurin-based cytotoxicity assay showing the cell viability results for Saos-2 cells exposed to extracts from MBG-based cements. The plate is divided into sections for BG0, BG2, and BG5. The color intensity reflects cell viability, with a more pronounced purple/pink indicating higher viability.

In conclusion, the cytotoxicity results show that all MBG-based cements, exhibit significant cytotoxic effects under the tested conditions. These findings underscore the need for further optimization of MBG compositions to reduce cytotoxicity while maintaining their therapeutic benefits.

4.9 Magnetic Hyperthermia Tests

Figure 20 presents the temperature change (ΔT(ºC)) observed during the magnetic hyperthermia tests of the BG0S, BG2S, and BG5S samples. The results show that the temperature increase for all samples remains relatively consistent, with ΔT values around 2.4°C for each sample. These results indicate that all samples produce a modest temperature increase under Alternating Magnetic Field (AMF) stimulation. However, this level of heating may not be sufficient for effective magnetic hyperthermia applications, where temperature rises of more than 5°C are typically required to induce localized hyperthermia capable of destroying cancer cells [13]. The consistent ΔT values across all samples suggest that the magnetic material present in the MBG matrix is responsible for the heating. However, the incorporation of copper, at least at the tested doping levels, does not significantly enhance the hyperthermia performance.

While the MBG show some potential for magnetic hyperthermia [13], the temperature rise observed in this test is relatively low. Further optimization of the SPION content might be necessary to achieve a more pronounced heating effect. This would improve the material's suitability for cancer treatment applications, where higher temperatures are crucial for therapeutic efficacy.

The slight variability in the observed temperature increase during the magnetic hyperthermia tests could also be attributed to potential errors during the synthesis of the SPIONs deposited on the BG. These errors may have affected the uniformity of SPION deposition and distribution within the MBG matrix, leading to reduced heat generation under AMF stimulation. Additionally, the variation in drying times—ranging from 4 to 7 days at 60°C—could have contributed to the inconsistency in temperature rise. Differences in drying durations might have resulted in uneven SPION dispersion or adhesion, affecting the overall homogeneity of the samples. These factors, combined with the insufficient initial dispersion of SPIONs, likely influenced the magnetic response and heat dissipation in the tested samples. As a result, the modest temperature increases observed may not be sufficient for effective magnetic hyperthermia applications, which typically require higher temperature rises for optimal cancer cell destruction.

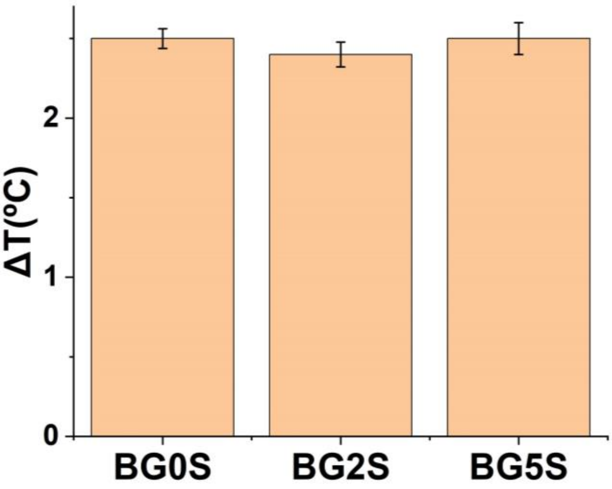

Figure 20 - Temperature change (ΔT) observed during the magnetic hyperthermia tests of BG0S, BG2S, and BG5S.

5

CONCLUSION AND FUTURE PERSPECTIVES

The research carried out in this thesis focused on the development of multifunctional injectable bone cements based on superparamagnetic MBGs containing SPIONs for bone cancer theranostics and regeneration. The results have demonstrated that the incorporation of SPIONs enables localized magnetic hyperthermia, which has the potential to contribute to cancer treatment by achieving the necessary localized heating. While the current results show that the temperatures achieved were slightly lower than optimal for therapeutic purposes, these results indicate a promising direction for further refinement.

Additionally, the doping of MBGs with copper ions (Cu^{2+}) significantly improved their antibacterial properties, particularly against Gram-positive bacteria like MRSA. Among the tested samples, BG5 exhibited the strongest antibacterial effect, particularly against MRSA, while BG0 and BG2 showed varying levels of activity. These results suggest that higher copper concentrations enhance antibacterial efficacy, though future tests with improved sample preparation are recommended to confirm these findings.

However, the cytotoxicity tests of MBG-based cements revealed significant cytotoxic effects. Saos-2 cell viability was well below 70% for all cement compositions (BG0, BG2, and BG5), classifying these samples as cytotoxic according to the ISO 10993-5 standard. This indicates that further optimization of the cement formulations is necessary to reduce cytotoxicity while maintaining their therapeutic properties. In contrast, the MBGs and passivated MBGs in powder form exhibited cell viability above 70%, showing that these materials in their non-cemented state are non-cytotoxic and biocompatible.

The dual role of SPIONs contributing to both mechanical properties and antibacterial activity suggests that their inclusion may require balancing to optimize ion release and achieve the desired biological outcomes in SPIONs@MBG. Further exploration of how SPIONs influence the kinetics of copper ion release will be critical to understanding the overall antibacterial efficacy of these composite materials.

Furthermore, the rheological properties and setting times of the bone cements were tailored to ensure optimal injectability and mechanical performance. The setting times observed in certain compositions, particularly BG2 with a ratio L/S of 1.50, align well with the clinical requirements for orthopedic applications, providing surgeons with the necessary handling time and ensuring rapid solidification post-application.

The results demonstrated that incorporating SPIONs into MBG cements significantly affects their rheological properties, particularly in terms of the setting process and final stiffness. While SPIONs generally slow down the setting time and reduce the stiffness, these effects vary depending on the SPION concentration and copper doping levels. For instance, SPIONs@MBG5 cement exhibited a final stiffness comparable to non-SPION cements samples, suggesting that higher copper content can mitigate the softening effect of SPIONs. Additionally, the liquid-to-solid (L/S) ratio plays a crucial role in determining the handling and final properties of the cement. Therefore, while SPIONs offer potential benefits for specific applications, their impact on the mechanical properties of the cement must be carefully evaluated and optimized according to the particular needs of the intended application.

In conclusion, the developed SPIONs@MBG-based injectable cements demonstrate significant potential as multifunctional materials for bone cancer treatment, combining localized hyperthermia with regenerative capabilities. However, the current formulations of the cements require further modification to reduce cytotoxicity. Future research should focus on in vivo studies and continued optimization of both the magnetic hyperthermia performance and biocompatibility of these injectable cements to ensure their clinical efficacy in bone regeneration and localized cancer therapy.

REFERENCES

[1] H. Chen and Y. Yao, “Progress of biomaterials for bone tumor therapy,” Jan. 01, 2022, *SAGE Publications Ltd*. doi: 10.1177/08853282211035236.

[2] S. Kargozar, M. Mozafari, S. Hamzehlou, H. W. Kim, and F. Baino, “Mesoporous bioactive glasses (MBGs) in cancer therapy: Full of hope and promise,” *Mater Lett*, vol. 251, pp. 241–246, Sep. 2019, doi: 10.1016/j.matlet.2019.05.019.

[3] S. Kaya, M. Cresswell, and A. R. Boccaccini, “Mesoporous silica-based bioactive glasses for antibiotic-free antibacterial applications,” Feb. 01, 2018, *Elsevier Ltd*. doi: 10.1016/j.msec.2017.11.003.

[4] S. Kargozar *et al.*, “Nanostructured bioactive glasses: A bird’s eye view on cancer therapy,” Nov. 01, 2023, *John Wiley and Sons Inc*. doi: 10.1002/wnan.1905.

[5] X. Yan *et al.*, “The in-vitro bioactivity of mesoporous bioactive glasses,” *Biomaterials*, vol. 27, no. 18, pp. 3396–3403, Jun. 2006, doi: 10.1016/j.biomaterials.2006.01.043.

[6] X. X. Yan *et al.*, “Mesoporous bioactive glasses. I. Synthesis and structural characterization,” *J Non Cryst Solids*, vol. 351, no. 40–42, pp. 3209–3217, Oct. 2005, doi: 10.1016/j.jnoncrysol.2005.08.024.

[7] Y. Z. Liu, Y. Li, X. Bin Yu, L. N. Liu, Z. A. Zhu, and Y. P. Guo, “Drug delivery property, bactericidal property and cytocompatibility of magnetic mesoporous bioactive glass,” *Materials Science and Engineering C*, vol. 41, pp. 196–205, Aug. 2014, doi: 10.1016/j.msec.2014.04.037.

[8] C. Wu and J. Chang, “Mesoporous bioactive glasses: Structure characteristics, drug/growth factor delivery and bone regeneration application,” 2012, *Royal Society*. doi: 10.1098/rsfs.2011.0121.

[9] X. Yan *et al.*, “The in-vitro bioactivity of mesoporous bioactive glasses,” *Biomaterials*, vol. 27, no. 18, pp. 3396–3403, 2006, doi: 10.1016/j.biomaterials.2006.01.043.

[10] S. Kaya, M. Cresswell, and A. R. Boccaccini, “Mesoporous silica-based bioactive glasses for antibiotic-free antibacterial applications,” Feb. 01, 2018, *Elsevier Ltd*. doi: 10.1016/j.msec.2017.11.003.

[11] S. S. Danewalia and K. Singh, “Bioactive glasses and glass–ceramics for hyperthermia treatment of cancer: state-of-art, challenges, and future perspectives,” Mar. 01, 2021, *Elsevier B.V.* doi: 10.1016/j.mtbio.2021.100100.

[12] C. Taşar and B. Ercan, “Fabrication and biological properties of magnetic bioactive glass nanoparticles,” *Ceram Int*, vol. 49, no. 8, pp. 12925–12933, Apr. 2023, doi: 10.1016/j.ceramint.2022.12.164.

[13] S. S. Danewalia and K. Singh, “Bioactive glasses and glass–ceramics for hyperthermia treatment of cancer: state-of-art, challenges, and future perspectives,” Mar. 01, 2021, *Elsevier B.V.* doi: 10.1016/j.mtbio.2021.100100.

[14] S. Kargozar, M. Montazerian, S. Hamzehlou, H. W. Kim, and F. Baino, “Mesoporous bioactive glasses: Promising platforms for antibacterial strategies,” Nov. 01, 2018, *Acta Materialia Inc*. doi: 10.1016/j.actbio.2018.09.052.

[15] R. Koohkan, T. Hooshmand, D. Mohebbi-Kalhori, M. Tahriri, and M. T. Marefati, “Synthesis, Characterization, and in Vitro Biological Evaluation of Copper-Containing Magnetic Bioactive Glasses for Hyperthermia in Bone Defect Treatment,” *ACS Biomater Sci Eng*, vol. 4, no. 5, pp. 1797–1811, May 2018, doi: 10.1021/acsbiomaterials.7b01030.

[16] Y. Z. Liu, Y. Li, X. Bin Yu, L. N. Liu, Z. A. Zhu, and Y. P. Guo, “Drug delivery property, bactericidal property and cytocompatibility of magnetic mesoporous bioactive glass,” *Materials Science and Engineering C*, vol. 41, pp. 196–205, Aug. 2014, doi: 10.1016/j.msec.2014.04.037.

[17] Y. Zhu *et al.*, “Magnetic mesoporous bioactive glass scaffolds: Preparation, physicochemistry and biological properties,” *J Mater Chem B*, vol. 1, no. 9, pp. 1279–1288, Mar. 2013, doi: 10.1039/c2tb00262k.

[18] Q. Shi, J. Wang, J. Zhang, J. Fan, and G. D. Stucky, “Rapid-setting, mesoporous, bioactive glass cements that induce accelerated in vitro apatite formation,” *Advanced Materials*, vol. 18, no. 8, pp. 1038–1042, Apr. 2006, doi: 10.1002/adma.200502292.

[19] C. Taşar and B. Ercan, “Fabrication and biological properties of magnetic bioactive glass nanoparticles,” *Ceram Int*, vol. 49, no. 8, pp. 12925–12933, Apr. 2023, doi: 10.1016/j.ceramint.2022.12.164.

[20] C. Wu *et al.*, “Copper-containing mesoporous bioactive glass scaffolds with multifunctional properties of angiogenesis capacity, osteostimulation and antibacterial activity,” *Biomaterials*, vol. 34, no. 2, pp. 422–433, Jan. 2013, doi: 10.1016/j.biomaterials.2012.09.066.

[21] X. Yan, C. Yu, X. Zhou, J. Tang, and D. Zhao, “Highly ordered mesoporous bioactive glasses with superior in vitro bone-forming bioactivities,” *Angewandte Chemie - International Edition*, vol. 43, no. 44, pp. 5980–5984, Nov. 2004, doi: 10.1002/anie.200460598.

[22] R. Koohkan, T. Hooshmand, D. Mohebbi-Kalhori, M. Tahriri, and M. T. Marefati, “Synthesis, Characterization, and in Vitro Biological Evaluation of Copper-Containing Magnetic Bioactive Glasses for Hyperthermia in Bone Defect Treatment,” *ACS Biomater Sci Eng*, vol. 4, no. 5, pp. 1797–1811, May 2018, doi: 10.1021/acsbiomaterials.7b01030.

[23] H. Luo *et al.*, “One-pot synthesis of copper-doped mesoporous bioglass towards multifunctional 3D nanofibrous scaffolds for bone regeneration,” *J Non Cryst Solids*, vol. 532, Mar. 2020, doi: 10.1016/j.jnoncrysol.2019.119856.

[24] S. S. Shendage, K. Gaikwad, K. Kachare, S. Kashte, and A. V. Ghule, “In vitro and in vivo study of copper-doped bioactive glass for bone regeneration application,” *Mater Chem Phys*, vol. 313, Feb. 2024, doi: 10.1016/j.matchemphys.2023.128789.

[25] C. M. Parler, J. A. Ritter, and M. D. Amiridis, “Infrared spectroscopic study of sol±gel derived mixed-metal oxides,” *ELSEVIER*, pp. 119–125, Feb. 2001, doi: https://doi.org/10.1016/S0022-3093(00)00401-4.

[26] Lohilahti Tilda, “FUNCTIONAL BIOCERAMICS FOR HY-PERTHERMIA-BASED BONE CANCER TREATMENT,” University, 2024.

[27] C. Y. Yang *et al.*, “Labeling of human mesenchymal stem cell: Comparison between paramagnetic and superparamagnetic agents,” *J Appl Phys*, vol. 105, no. 7, pp. 1–4, 2009, doi: 10.1063/1.3072821.

[28] X. Wang *et al.*, “Biocomposites of copper-containing mesoporous bioactive glass and nanofibrillated cellulose: Biocompatibility and angiogenic promotion in chronic wound healing application,” *Acta Biomater*, vol. 46, pp. 286–298, Dec. 2016, doi: 10.1016/j.actbio.2016.09.021.

[29] S. Akhtach, Z. Tabia, K. El Mabrouk, M. Bricha, and R. Belkhou, “A comprehensive study on copper incorporated bio-glass matrix for its potential antimicrobial applications,” *Ceram Int*, vol. 47, no. 1, pp. 424–433, Jan. 2021, doi: 10.1016/j.ceramint.2020.08.149.

[30] A. Gholami, F. Mohammadi, Y. Ghasemi, N. Omidifar, and A. Ebrahiminezhad, “Antibacterial activity of SPIONs versus ferrous and ferric ions under aerobic and anaerobic conditions: A preliminary mechanism study,” *IET Nanobiotechnol*, vol. 14, no. 2, pp. 155–160, Apr. 2020, doi: 10.1049/iet-nbt.2019.0266.

[31] Ö. Demir-Oğuz, A. R. Boccaccini, and D. Loca, “Injectable bone cements: What benefits the combination of calcium phosphates and bioactive glasses could bring?,” Jan. 01, 2023, *KeAi Communications Co.* doi: 10.1016/j.bioactmat.2022.04.007.

[32] E. Şahin and D. M. Kalyon, “The rheological behavior of a fast-setting calcium phosphate bone cement and its dependence on deformation conditions,” *J Mech Behav Biomed Mater*, vol. 72, pp. 252–260, Aug. 2017, doi: 10.1016/j.jmbbm.2017.05.017.

[33] E. Şahin, “Calcium Phosphate Bone Cements,” in *Cement Based Materials*, H. El-Din M. Saleh and R. Rahman, Eds., InTech, 2018, ch. 12, pp. 1–31. doi: 10.5772/intechopen.74607.

[34] F. Baino, “Copper-Doped Ordered Mesoporous Bioactive Glass: A Promising Multifunctional Platform for Bone Tissue Engineering,” *Bioengineering*, vol. 7, no. 2, p. 45, May 2020, doi: 10.3390/bioengineering7020045.

A

APPENDIX A

A.1 Materials

Tetraethyl orthosilicate (TEOS, 98%) (C8H20O4Si, Mw = 208.33 g/mol, CAS 78-10-4) was obtained from Sigma-Aldrich. Triethyl phosphate (TEP, ≥ 99.8 %) (C4H15O4P, Mw = 182.15 g/mol, CAS 78-40-0) was obtained from Sigma-Aldrich. Hydrochloric acid (HCl, CAS 7647-01-0) was obtained from Honeywell. Copper(II)-chlorid (CuCl2·2H2O, Mw = 170.48 g/mol, CAS 10125-13-0) was obtained from E. Merck, Darmstadt. Poly(ethylene glycol)-block-poly(propyleneglycol)-block-poly(ethylene glycol) Pluronic® P-123 (CAS 9003-11-6) was obtained from Sigma-Aldrich. Ethanol absolute anhydrous (C2H5OH, Mw = 46 g/mol, CAS 64-17-5) was obtained from CARLO ERBA Reagents. Millipore water was used for the synthesis of SDBG.

A.2 Characterization

For the particle size measurements, the Mastersizer Hydro 2000MU from Malvern Instruments was used, an instrument that allows the particle size characterization of particle suspensions (with dimensions between 20 nm and 2,000 µm) with a wet dispersing unit. To measure particle size, this instrument uses the laser diffraction technique (laser granulometer). It measures the intensity of light scattered when a laser beam interacts with scattered particles in the sample. This data is then analyzed to calculate the particle size distribution from the scattering pattern generated. Particle size is expressed as the diameter of an equivalent volume sphere.

The structural characterization of the samples was assessed by X-ray diffraction (XRD) using an MPD X'Pert PRO powder diffractometer from PANalytical with a Cu Kα radiation source (λ = 1.540598 Å) equipped with a 1D X'Celerator detector. The XRD measurements were performed in the range of 10 to 65° (2θ) in the Bragg–Brentano configuration, with a scanning step size of 0.033°.

For BET analysis, the samples were previously degassed at 200 °C for at least 6 hours. They were analyzed using nitrogen at 77 K as the adsorption gas. The instrument is a Micromeritics, model ASAP 2010.

STEM observations were performed with a Hitachi HF5000 field-emission scanning transmission electron microscope (Mito, Japan) operated at 200 kV. A drop of the sonicated dispersions was deposited onto 200-mesh lacey-carbon copper grids and allowed to dry before observation.

FT-IR data were recorded using an Attenuated Total Reflectance (ATR) sampling accessory equipped with a single bounce diamond crystal on a Thermo Nicolet SummitX Spectrometer. The spectra were acquired with a 45° incident angle in the range of 4000–400 cm^{-1} and with a 4 cm^{-1} resolution.

The rheological characterization of SiO_2-CaO-P_2O_5 mixtures was performed with a Malvern Gemini Hrnano Rotational Rheometer, equipped with a Peltier plate for temperature control (±0.01 °C). A parallel-plate geometry, with a diameter of 20 mm and a gap of 1.0 mm was used. Oscillatory shear measurements were performed to evaluate the storage G′ and the loss G″ moduli within the linear viscoelastic regime (LVR) to guarantee that moduli are strain independent. Amplitude strain sweep was performed at 6,28 rad/s in the range of 0.01 to 100% and the angular frequency sweep measurements were carried out under a constant strain of 0.1% in the frequency range of 0.1 to 100 Hz, at 25 and 37 °C. The kinetics of setting transition was evaluated though a single frequency test, at 0.1, 1, 10 and 100 Hz, a long time, where the G' and G'' behavior was evaluated, at 37°C and imposing a 0.1% strain. A solvent trap was used to minimize evaporation in the single frequency tests.

The DC magnetic properties were measured using a 7 T SQUID magnetometer (S700X; Cryogenic Ltd.). Zero-field cooled (ZFC) and field-cooled (FC) measurements were conducted by cooling the sample down to 5K, either in the absence of an external field (ZFC) or under an applied field of 100 Oe (FC). The magnetic measurements were recorded over a temperature range of 5–320K. Additionally, isothermal magnetization curves were obtained at temperatures of 10K and 320K for magnetic fields up to 5 T.

A.3 Evaluation of cytotoxicity and antibacterial activity

Cytotoxicity was evaluated using Saos-2 cells cultured in McCoy's 5A medium. The *in vitro* cytotoxicity assessment was carried out using the extract method, following the guidelines outlined in the International Standard ISO 10993-5 'Biological evaluation of medical devices—Part 5: Tests for in vitro cytotoxicity' [21].

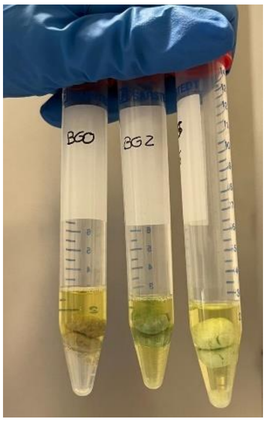

Figure A1 - Image showing the MBG-based cement samples in McCoy's 5A medium for extract preparation used in cytotoxicity testing. From left to right: BG0, BG2, and BG5.

To evaluate the biological activity, an altered standard broth microdilution method with materials extracts was performed using the ISO 20776-1 guidelines to determine Minimum Inhibitory Concentration (MIC) values of the doped MBG and SPIONs@MBG for 2 strains, Gram-negative E.coli and Gram-positive bacteria MRSA. The results were obtained based on the transparency and opacity of each well.

To evaluate the biological activity of the MBG-based cements, the Kirby-Bauer qualitative method was employed. Two bacterial strains were tested: Gram-negative E. coli and Gram-positive MRSA. To prepare approximately 10 MBG-based cement samples of 0.5g each with a L/S ratio of 1.5, about 69g of the solid phase was mixed with 5ml of the liquid phase. The result can be observed in Figure A2.

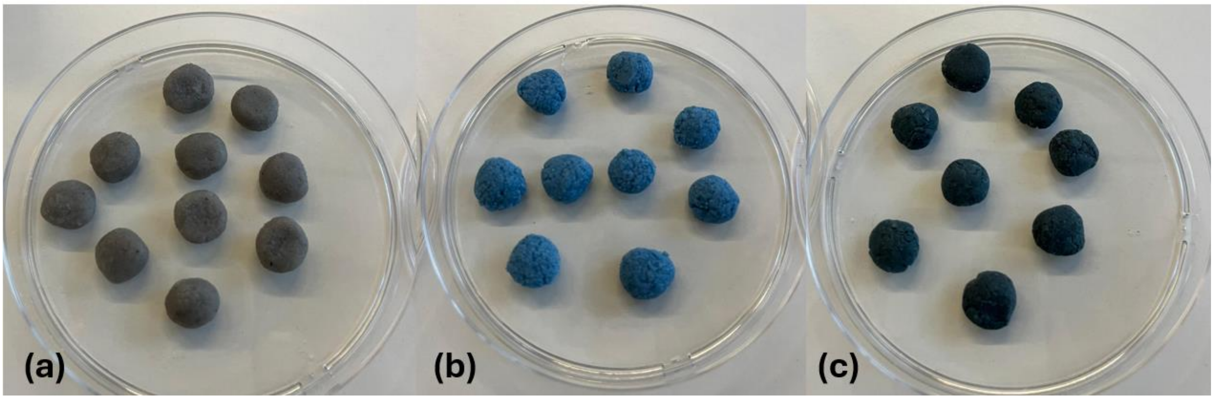

Figure A2 - MBG-based cement samples of 0.5g each with a liquid-to-solid (L/S) ratio of 1.5. (a) MBG0-based cement, (b) MBG2-based cement, and (c) MBG5-based cement.

A.4 Nitrogen Sorption Isotherms

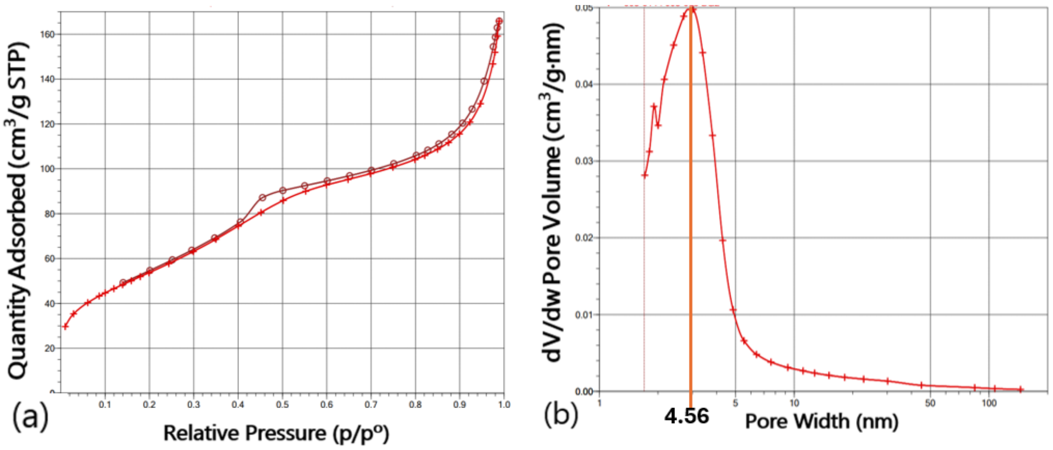

Figure A3 - (a) Isotherm Linear Plot of the sample BG2; (b) BJH Adsorption dV/dw Pore Volume of the sample BG2.

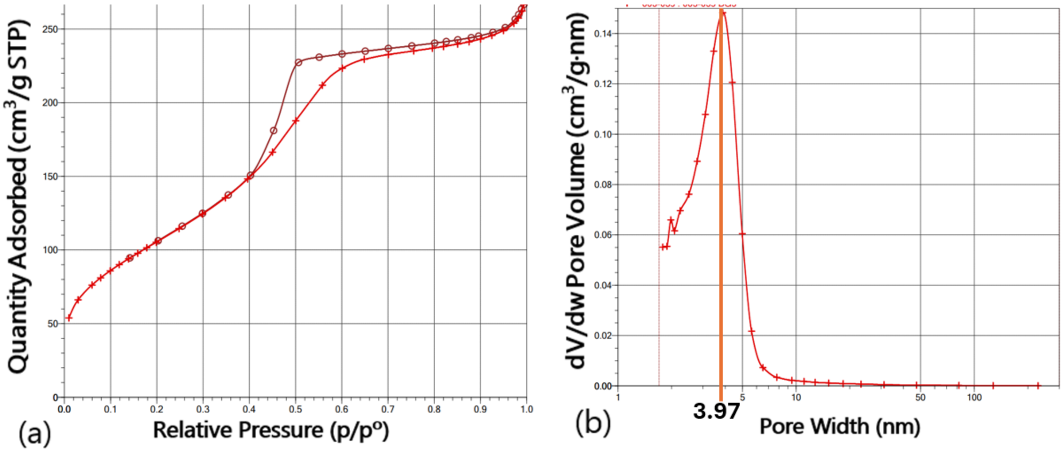

Figure A4 - (a) Isotherm Linear Plot of the sample BG5; (b) BJH Adsorption dV/dw Pore Volume of the sample BG5.

A.5 Structural Analysis via Electron Microscopy

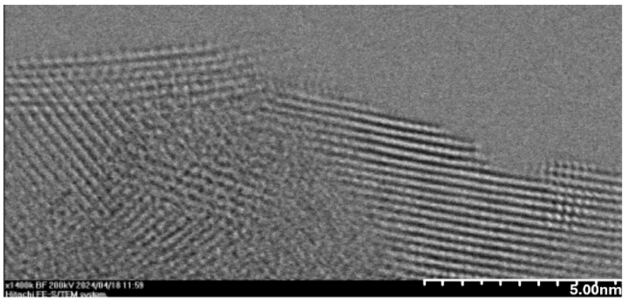

Figure A5 - STEM Image obtained from the BG2 sample

A.6 Evaluation of bioactivity

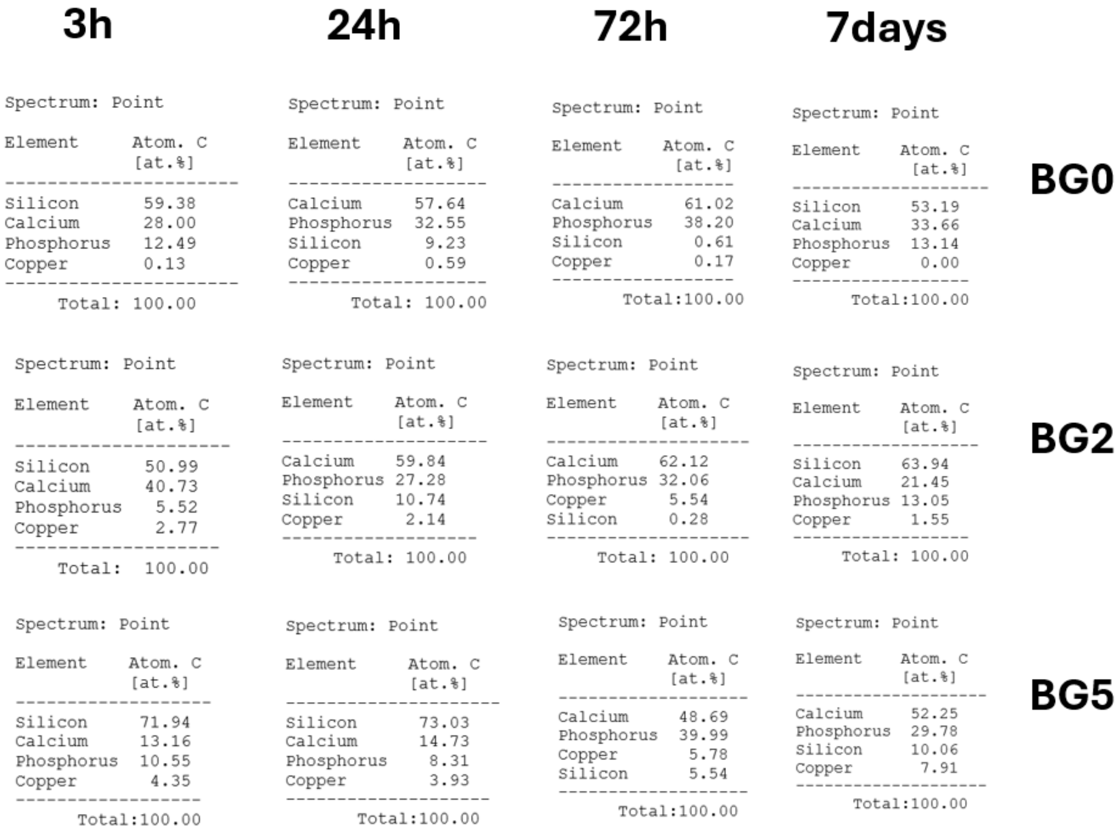

```
Spectrum: Point

Element      Atom. C
             [at.%]
----------------------
Silicon       59.38
Calcium       28.00
Phosphorus    12.49
Copper         0.13
----------------------
     Total: 100.00
```

```
Spectrum: Point

Element     Atom. C
             [at.%]
-------------------
Calcium      57.64
Phosphorus   32.55
Silicon       9.23
Copper        0.59
-------------------
      Total: 100.00
```

```
Spectrum: Point

Element     Atom. C
             [at.%]
-----------------
Calcium      61.02
Phosphorus   38.20
Silicon       0.61
Copper        0.17
-----------------
       Total:100.00
```

```
Spectrum: Point

Element     Atom. C
             [at.%]
-------------------
Silicon      53.19
Calcium      33.66
Phosphorus   13.14
Copper        0.00
-----------------
     Total:100.00
```

```
Spectrum: Point

Element      Atom. C
             [at.%]
--------------------
Silicon       50.99
Calcium       40.73
Phosphorus     5.52
Copper         2.77
-------------------
    Total:  100.00
```

```
Spectrum: Point

Element     Atom. C
             [at.%]
-------------------
Calcium     59.84
Phosphorus 27.28
Silicon     10.74
Copper       2.14
------------------
     Total: 100.00
```

```
Spectrum: Point

Element     Atom. C
             [at.%]
-------------------
Calcium     62.12
Phosphorus 32.06
Copper       5.54
Silicon      0.28
-------------------
     Total: 100.00
```

```
Spectrum: Point

Element     Atom. C
             [at.%]
------------------
Silicon     63.94
Calcium     21.45
Phosphorus 13.05
Copper       1.55
-----------------
     Total: 100.00
```

```
Spectrum: Point

Element     Atom. C
            [at.%]
------------------
Silicon      71.94
Calcium      13.16
Phosphorus   10.55
Copper        4.35
-----------------
     Total:100.00
```

```
Spectrum: Point

Element      Atom. C
             [at.%]
--------------------
Silicon       73.03
Calcium       14.73
Phosphorus     8.31
Copper         3.93
-------------------
     Total:100.00
```

```
Spectrum: Point

Element     Atom. C
            [at.%]
------------------
Calcium      48.69
Phosphorus  39.99
Copper        5.78
Silicon       5.54
------------------
      Total:100.00
```

```
Spectrum: Point

Element      Atom. C
             [at.%]
-------------------
Calcium       52.25
Phosphorus   29.78
Silicon      10.06
Copper        7.91
-------------------
     Total:100.00
```

Figure A6 - Elemental composition of bioactive glass samples (BG0, BG2, and BG5) at different immersion times (3 hours, 24 hours, 72 hours, and 7 days) in simulated body fluid (SBF), obtained through energy-dispersive X-ray spectroscopy (EDS).

A.7 Simulated body fluid (SBF)

Materials:

- Millipore water
- Sodium chloride (NaCl, Sigma-Aldrich)
- Sodium bicarbonate ($NaHCO_3$, Sigma-Aldrich)
- Potassium chloride (KCl, Sigma-Aldrich)
- Potassium phosphate dibasic trihydrate ($K_2HPO_4 \cdot 3H_2O$, Sigma-Aldrich)
- Magnesium chloride hexahydrate ($MgCl_2 \cdot 6H_2O$, Sigma-Aldrich)
- Hydrochloric acid (1M HCl, Sigma-Aldrich)
- Calcium chloride ($CaCl_2$, Sigma-Aldrich)

- Sodium sulfate (Na_2SO_4, Sigma-Aldrich)
- Tris(hydroxymethyl)aminomethane ($NH_2C(CH_2OH)_3$, Sigma-Aldrich)

Methods:

In a 1 L flask, add 750 mL of Millipore water and maintain constant magnetic stirring at 37 ºC. Once the water reaches a stable temperature of 37 ºC, begin adding the reagents in the following order:

1. 7.996 g of NaCl
2. 0.350 g of $NaHCO_3$
3. 0.224 g of KCl
4. 0.228 g of $K_2HPO_4 \cdot 3H_2O$
5. 0.305 g of $MgCl_2 \cdot 6H_2O$
6. 40 mL of 1M HCl
7. 0.278 g of $CaCl_2$
8. 0.071 g of Na_2SO_4
9. 6.057 g of $NH_2C(CH_2OH)_3$

Once all the reagents were fully dissolved, the pH was adjusted to 7.4 using HCl. The final volume was then brought up to 1000 mL by adding additional Millipore water.

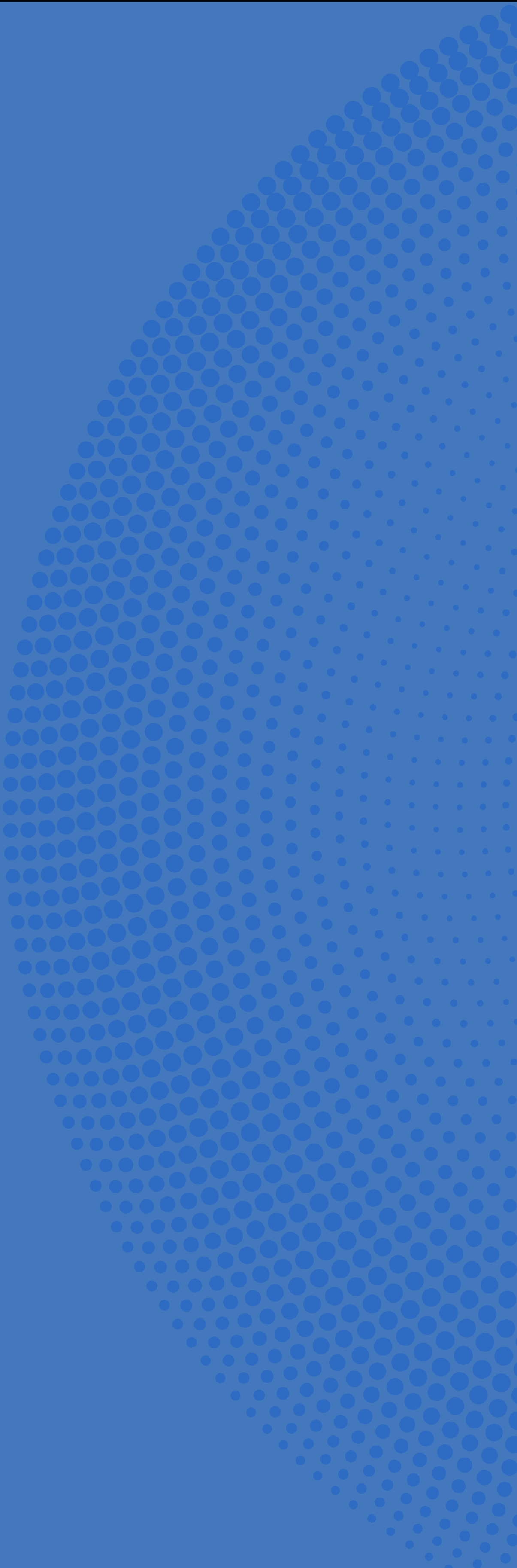

2024

FRANCISCA CRUZ

MULTIFUNCTIONAL SUPERPARAMAGNETIC MESOPOROUS BIOACTIVE GLASS-BASED
INJECTABLE BONE CEMENTS FOR CANCER THERANOSTICS AND BONE REGENERATION

NOVA SCHOOL OF
SCIENCE & TECHNOLOGY